FINAL PROJECT REPORT TO THE DEPARTMENT OF ENERGY (DOE)

SUBMITTED: December, 2009

Disclaimer: This report does not contain any proprietary, confidential, or otherwise restricted information.

<u>Project Title:</u> Development of Novel PEM Membrane and Multiphase CFD Modeling of PEM Fuel Cell

(Kettering University's Fuel Cell Project)

Project Director/Principal Investigator: K. Joel Berry (Primary Contact)

Consortium/teaming Members: Susanta K. Das, Panini K. Kolavennu, Jamie Hedrick, Ali R. Zand and Lars G. Beholz

Center for Fuel Cell Systems and Powertrain Integrations, Kettering University
1700 West Third Avenue
Flint, MI 48504
Phone: (810) 762-7833; Fax: (810) 762-7860
E-mail: jberry@kettering.edu

DOE Technology Development Manager: Kathi Epping
Phone: (202) 586-7425; Fax: (202) 586-9811
E-mail: Kathi.Epping@ee.doe.gov

DOE Project Officer: David Peterson
Phone: (303) 275-4956; Fax: (303) 275-4788
E-mail: David.Peterson@go.doe.gov

Contract Number: DE-FG36-06GO86056

Project Start Date: July 1, 2006
Project End Date: June 30, 2009

Table of contents

Contents **Page number**

Executive Summary:

The objectives of this project were three-folds: (i) develop a novel PEM fuel cell membrane, (ii) develop a multiphase CFD flow model for PEM fuel cell and (iii) develop a control strategy for PEM fuel cell stack.

In this project, using patented side-chain of polymer backbone modification technology, a novel approach to the design and fabrication of proton exchange membrane (PEM) has been developed whereby a non-structural polymer fabricated with high proton exchange capacity was bound to an inert polymer matrix. The patented fabrication techniques used here allow greater flexibility in PEM design. Results related to proton exchange performance of this novel PEM is presented here. The proton exchange material described herein is a ter-polymer composed of various ratios of monomers. These materials were bound to an inert ethylene-tetrafluoroethylene (ETFE) copolymer mesh that had been rendered adhesive using patented hydroxylation technique in a two-step water-borne process. The basic characteristics of the new membranes were compared to those of commercial membrane, Nafion® 212. An aqueous two-cell testing unit is utilized by which the rate of protons transferred from one cell through the membrane into the other cell was determined by monitoring the change in pH of the cells. Laboratory scale test results indicated that the new membrane could transfer protons approximately 10 times faster per unit area compared to Nafion® 212 under the test conditions utilized at 80^{o}C. Results using industry standard test protocols also show performance improvements of our PEM membrane from batch 1 to batch 2. In addition to improvement in induction time and reduced resistance, the new membrane conducts protons at reduced membrane water content compared to Nafion® 212. The objectives of improved proton conductivity through a proton exchanging polymer matrix cast onto a very mechanically and chemically stable robust ETFE mesh were achieved by separating different PEM requirements and distributing them among different PEM polymer matrices. In the present study, many of the structural and mechanical requirements were met by the ETFE mesh while the proton exchange polymer media was designed to optimize proton transfer capacity. Although the materials used to prepare these hybrid membranes were purchased from specialty chemical and polymer companies, the cost of ETFE (ethylene-tetrafluoroethylene) used in the current study was approximately \$353 m^{-2} and that of the chemicals was under \$20.00 m^{-2}. Manufacturing costs are also relatively low and the preparation and casting of the membrane cocktail onto the mesh did not require any expensive special equipment. It is thus anticipated that larger scale manufacturing of our SAS (**s**tyrene-**a**crylic acid-vinyl**s**ulfonate) type PEMs will be significantly less expensive and economically feasible than the manufacture of Nafion®-type membranes.

To understand heat and water management phenomena better within an operational proton exchange membrane fuel cell's (PEMFC) conditions, a three-dimensional, two-phase computational fluid dynamic (CFD) flow model has been developed and simulated for a complete PEMFC. Both liquid and gas phases are considered in the model by taking into account the gas flow, diffusion, charge transfer, change of phase, electro-osmosis, and electrochemical reactions to understand the overall dynamic behaviors of species within an operating PEMFC. The CFD model is solved numerically under different parametric conditions in terms of water management issues in order to improve cell performance. The results obtained from the CFD two-phase flow model simulations show improvement in cell performance as well as water management under PEMFCs operational conditions as compared to the results of a single phase flow model available in the literature. The quantitative information obtained from the two-phase model simulation results helped to develop a CFD control algorithm for low temperature PEM fuel cell stacks which opens up a route in designing improvement of PEMFC for better operational efficiency and performance.

Project Objectives

- Develop new and novel proton conducting membrane materials capable of conducting protons at low relative humidity (RH), withstanding temperatures in excessive of 110^{o}C and provide electrical insulation.
- Quantify extent of membrane performance enhancement compared to peer materials available in the market place.
- Reduce materials cost and develop simple manufacturing processes.
- Improve durability, dimensional stability, and thermal stability.
- Develop computational fluid dynamics (CFD) multiphase porous flow models to understand thermal and water-transport phenomena in proton exchange membrane (PEM) fuel cell.

Technical Barriers addressed

This project addresses the following technical barriers from the Fuel Cells section of the Hydrogen, Fuel Cells and Infrastructure Technologies (HFCIT) Program Multi-Year Research, Development and Demonstration Plan:

(A) Performance
(B) Cost
(C) Durability
(E) Thermal and Water Management

Technical Targets

This project is conducting fundamental studies to develop a new class of PEM materials capable of conducting protons at low relative humidity. The multiphase CFD model will help to understand underlying physics related to water and thermal management in PEM fuel cell. If successful, insights gained from these studies will be applied toward the design and manufacturing of advanced membrane materials that meet the following DOE 2010 membrane materials targets:

- Cost: \$20/m^2
- Conductivity at operating temperature ($\leq$120^{o}C): 0.1 S/cm
- Humidity range $\leq$ 50%
- Area specific resistance: 0.02 Ohm/cm^2
- Durability with cycling: at operating temperature ($\leq$80^{o}C) – 5,000 hours
- Multiphase CFD porous flow model for designing improved water and thermal management strategies

Accomplishments

- Identified inexpensive membrane materials and developed simple manufacturing process capable of producing proton conducting membrane materials at a cost of 60% below the DOE targets for 2010.
- Increased Proton Conductivity: In-house laboratory test shows that average 10 times increase in proton conductivity compared to peer materials (Nafion® 212) at 80^{o}C. Third party (BekkTech) test results show improvement of membrane conductivity in our updated version (batch 2) of our membrane sample.

- Reduced Resistance: In-house laboratory test shows 71% lower resistance per unit area than peer (Nafion® 212) materials at 80°C (results reported to DOE last year).
- Reduced Induction Time: Induction time (time required to start proton transfer) is 70% lower than Nafion® 212.
- Low Membrane Water Content: Membrane able to conduct protons at low water content i.e. at low relative humidity compared to peer materials (Nafion® 212) at 80°C.
- Developed and simulated multiphase porous flow model for CFD analysis of a single PEM fuel cell.
- Improved Prediction: Using two-phase CFD model results we developed a 3D control strategy for improved prediction of fuel cell stack performance while meeting the power demand.

Action Plan/Task Schedule

Task	Project Milestones	Task Completion Date				Progress Meter
		Original Planned	Revised Planned	Actual	% Done	
1	Apply patented BEI-TECH process to add sulfonate functionality to inert polymer and measure proton conductivity. The anticipated result will be an inexpensive, robust polymer modified to have proton exchange characteristics similar to Nafion.	FY06, C.1	FY07,C.1	FY07, C.1	100%	Completed
2	**a)** Literature review and model formulation for porous media two-phase flows. **b)** Expand CFD finite element code for porous media two-phase flows (COMSOL).	FY07-08, C.4	FY07-08, C.4	FY07-08, C.4	**a)** 100% **b)** 100%	Completed.
3	Modify tethered polymer to include polymer cross-linking. The anticipated result is the formation of more contiguous proton transport channels while further increasing membrane durability.	FY07-08, C.2, C.3	FY08-09, C.2, C.3	FY08-09, C.2, C.3	100%	Completed
4	Develop and evaluate objective function and determine design surface map.	FY07-08, C.4	FY08-09, C.4	FY08-09, C.4	100%	Completed
5	Milestone: Expand/evaluate DOE sensitivity matrix for 3D porous model. Milestone: Validate numerical model through experimental testing.	FY08, C.4	FY09, C.4	FY09, C.4	100%	Completed
6	Project Management	12/31/09			100%	Completed

Project Activities

1. Development of new and novel proton conducting membrane materials

1.1: Introduction

Currently, a benchmark commercially produced and widely used proton exchange membrane (PEM) for fuel cell applications is Nafion® [1]. Nafion® has a number of limitations such as an operating temperature range of 50^oC~90^oC [2] undesirable gas permeability - on the order of 10^{-6} cm^2/s [3], which results in decreased fuel cell performance, limited operational hydration range [2-3] and high cost, US $800 per m^2 [1-3]. Additionally, Nafion® (polymer membrane) is easily degraded under high power and during on/off cycling. As such, polymer membranes need considerable improvement. Another concern is to thoroughly understand the water production and proton conduction mechanisms to minimize cathode electrode flooding and to ensure proper membrane hydration. The essential requirements of PEMs for fuel cell applications include the following: (i) high proton conductivity, (ii) minimal thickness (to minimize resistance resulting in fuel cell's ohmic drop), (iii) high thermal stability, (iv) excellent mechanical properties (strength, flexibility, and processability), (v) excellent chemical stability, (vi) low water drag, (vii) rapid adjustment of fast kinetics for electrode reactions, (viii) low or minimal gas permeability, and finally (ix) low cost and high availability.

In this project, using patented [4-5] polymer surface modification technology, a novel approach to the design and fabrication of PEMs has been developed whereby a non-structural polymer fabricated for proton exchange capacity is bound to an inert polymer matrix. This fabrication technique separates the proton exchange and structural requirements of the PEM allowing greater flexibility in proton exchange membrane design. To benchmark the performance of the membranes, we developed a theoretical model [6] to quantify several physical quantities such as proton exchange capacity (conductivity), resistance, induction time, and membrane water content. The results suggest a new route to fabricate cost-effective PEMs for fuel cell applications wherein one may focus more on the proton exchange capacity of the membrane allowing the structural properties of the membrane to be considered separately. We tested our membrane's performances using both laboratory-based method and industry-standard test protocols.

1.2: Approach

- Use an inert, robust, mechanically and dimensionally stable polymer mesh that may be chemically modified on the surface to render it adhesive or chemically reactive.
- Use patented technology to prepare a proton exchange polymer media that has been designed primarily to have high proton exchange capability.
- Cast the proton exchange polymer media onto the robust polymer support to prepare the hybrid proton exchange membrane.
- Alter the composition of the proton exchange polymer media to optimize proton transport.
- Compare the performance of new PEM materials with the peer materials such as Nafion® 212.

1.3: Materials and Methods

1.3.1: Materials

Ethylene-tetrafluoroethylene (ETFE) mesh (70µm nominal aperture, 66.7 threads/square inch, 70 µm monofilament diameter, 21% open area) was purchased from Goodfellow Corporation, Oakdale, PA, U.S.A.. 15% sodium hypochlorite and 85% phosphoric acid were purchased from PVS Nolwood, Detroit, MI, U.S. A.. All other chemicals and polymers were purchased from Sigma-Aldrich Corporation, St. Louis, MO, U.S.A. unless otherwise indicated.

1.3.2: Manufacturing Procedures

The manufacturing process consists of three steps; (i) surface modification of ETFE mesh by chemical treatment, (ii) preparation of proton exchange polymer and finally (iii) casting the proton exchange polymer onto the surface modified ETFE mesh to develop the hybrid PEM. Firstly, ETFE mesh was chlorinated by immersion in 15% sodium hypochlorite into which phosphoric acid was carefully added until constant light bubbling was achieved. The solution was then stirred overnight. After chlorination, the mesh was rinsed with water and subsequently hydroxylated by placing in an aqueous 1M sodium hydroxide (NaOH) solution overnight. This method resulted in the preparation of a hydroxylated surface on the ETFE mesh rendering it adhesive or optional chemically reactive as shown in Figure 1.

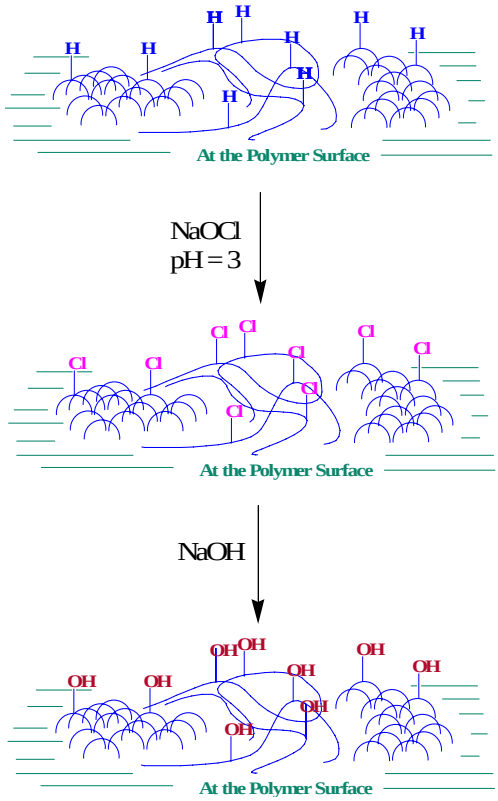

Figure 1: Schematic of ETFE functionalization processes by BEI-Tech patented technology.

Secondly, the proton exchange polymer was prepared by adding the desired proportions of monomers - acrylic acid, styrene, and vinyl sulfonic acid to a vial followed by a small amount of benzoyl peroxide to act as a radical initiator. For example (exact ratios are not mentioned here for proprietary reasons), 5 ml of acrylic acid, 8 ml of styrene, 0.1 ml of vinylsulfonic acid and 11.0 mg of benzoyl peroxide would form a typical membrane cocktail. Enough ethanol was then added to achieve a homogeneous solution. This solution was then very slowly heated in a sand bath to a temperature between 100^{o}C to 110^{o}C. The reaction time, monomer concentration and percentage of conversion during polymerization are given in Table 1. After polymerization was complete, it was removed from the sand bath and allowed to cool at ambient temperature (25^{o}C). After cooling, the polymer was isolated and then re-dissolved in ethanol to prepare the solution cocktail into which the hydroxylated ETFE mesh was placed. The ETFE mesh now coated with the proton exchange polymer was then spun dry in a centrifuge. The new **s**tyrene-**a**crylic acid-vinyl**s**ulfonate (SAS) proton exchange polymer will subsequently be referred to as "SAS" polymer. This casting procedure was repeated with drying in between each casting step. The new SAS PEM has the general structure indicated in Figure 2a wherein the mechanically fragile SAS polymer matrix that exchanges protons, denoted by light green, was cast onto the mechanically stable hydroxylated ETFE mesh to form the final SAS PEM shown in Figure 2b.

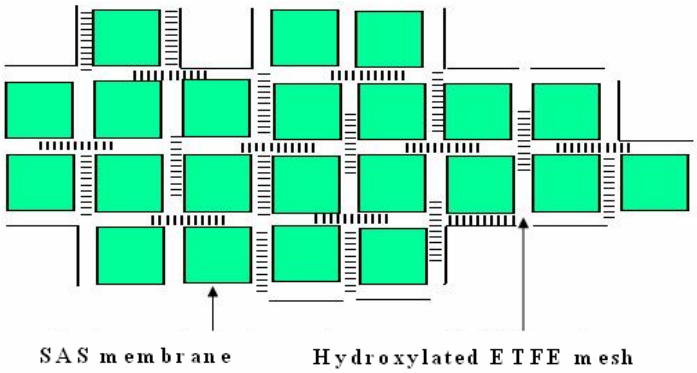

(a)

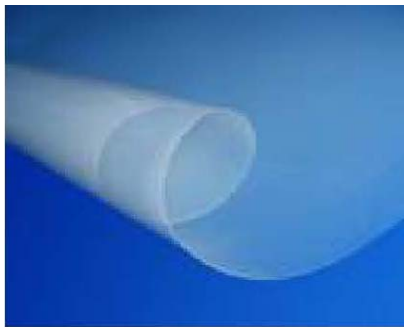

(b)

Figure 2: (a) General structure of proton exchange polymer cast onto ETFE mesh, and (b) final product of SAS proton exchange membrane.

Since only the surface structure of the ETFE was modified through patented chemical processing, it was anticipated that the ETFE mesh would provide the structural support of the new

SAS PEMs whereas the SAS proton exchange polymer would act as an efficient proton exchange media. Initial tests demonstrated [6] that increased sulfonate functionality (increased vinylsulfonic acid) to the polymer backbone provides increased proton conductivity by allowing the formation of proton migration channels throughout the polymer membrane.

Table 1: Reaction time, monomer concentration and percentage of conversion during polymerization.

Name of monomer	Reaction time	Concentration	% of conversion
acrylic acid	24.3 h	40%	27.8
styrene		100%	26.4
vinyl sulfonic acid		70%	45.8

1.4: Membrane Performance Measurement

1.4.1: Measurement of proton transfer rate and membrane resistance

In this study, an aqueous two-cell testing unit (schematic is shown in Figure 3) was used wherein the rate of proton transfer from one cell through the membrane into the other cell was determined by monitoring the change in pH of the cells. The proton exchange membrane (PEM) was placed into the PEM holder between the two cells. To ensure that transfer of protons from one cell to the other did not occur without passing through the PEM, silicone grease was applied around the outer edge of the PEM holder.

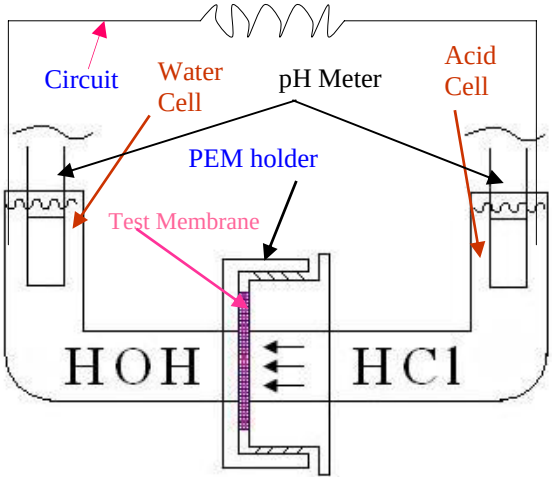

Figure 3: Schematic of water-borne two-cell unit with PEM holder used to test proton exchange capacity**.** PEM indicated in purple color at the center.

First, equal amount of de-ionized water was added to each cell. Then cells were allowed to equilibrate so that the water on each side of the membrane achieved the same depth. A pH meter was fitted into each cell to accurately record the pH readings. After the pH meters reached in equilibrium, simultaneously 20 drops of de-ionized water was added to the left cell and 20 drops of

20% HCl solution were added to the right cell using same size pipette. This procedure was used to ensure the volume of liquid in each cell remained the same so that there would be no liquid forced through the membrane by pressure differences (i.e. avoided pressure driven flow). A half-cell voltage circuit with 1.3583V for Cl^- [7-8] was established between the water and acid cells in order to maintain electrical neutrality. The half-cell circuit is commonly used in electroplating. By establishing half-cell reaction circuit between the cells we assured high proton concentrations in the acid cell. The chloride ion in the acid cell becomes chlorine gas and protons transferred in the water cell become hydrogen gas with the help of half-cell voltage circuit. The half-cell voltage circuit electron activity is shown below:

$$\textbf{Acid Cell: } 2HCl \leftrightarrow 2H^+ + 2Cl^-$$

$$2Cl^- \longrightarrow 2e^- + Cl_2$$

$$\textbf{Water Cell: } H^+ + 2e^- \longrightarrow H_2$$

Figure 4 illustrates the complete experimental set-up to measure change in pH of the cells. The initial pH and temperature of both cells were recorded immediately. Since there will be a negative gradient in the concentrations of protons between two cells, thus protons should moved from the acid cell through the PEM to the water cell. pH readings of both acid cell and water cell were then taken at a regular interval, usually every 2-5 minutes, until constant pH values were achieved in both cells. All measurements were carried-out without stirring under quiescent conditions. After collecting sufficient readings, the experiment was terminated. Experiments were repeated with the same set-up and initial conditions to test the performance of each of the membrane types reported here.

Figure 4: Membrane resistance test apparatus: two-cell method. Acid cell, water cell and test membrane sections are labeled and indicated by arrow sign. pH meter is attached into each of the cells and pH is recorded at a regular time interval through the monitor.

The total proton concentration was calculated using the theoretical model based on the rate of transfer of protons in the water cell through the membrane [6] given as:

$$C_w(t) = C_f\left(1 - 0.3679\left[\frac{C_f - C_0}{C_f}\right]\right) \quad (1)$$

where C_0 and C_f are the values of proton concentration at time $t = 0$ and at time $t = \infty$ respectively, and $C_w(t)$ is the proton concentration in the water cell (see Figure 4). The values of C_0 and C_f were determined from the experiment shown in Figure 4.

Finally, the exact resistance of the membrane was calculated by subtracting the solution's resistance from the total resistance [6] as given by:

$$R = \left(r - \frac{1}{\tau_{am}} - \frac{1}{\tau_{mw}}\right) = 2t = T \quad (2)$$

where R is the membrane resistance, r is the total resistance, τ_{aw} and τ_{mw} are the interfacial/solution resistances, t is the instant of time and T is the total time.

1.4.2: pH measuring process and calculation of proton concentration

a) At the beginning of the experiment, the pH of both the acid cell and water cell were measured.
b) Once the experiment was started, the measurement of pH was done at a regular interval of time.
c) The experiment was terminated after the pH of both cells had reached equilibrium.
d) The final value of pH in each cell (acid and water) was recorded.
e) The concentration of protons was then obtained using the relation: $\left[H^+\right] = 10^{-\mathrm{pH}}$.

1.5: Results and discussions (Membrane development)

The patented technology [4-5], used in this study as described in Figure 5, resulted in the attachment of hydroxyl groups onto the polyethylene portions of the ETFE copolymer onto which the proton exchange matrices attached. As shown in Figure 5, according to [4-5], through BT process-A (details are not discussed due to proprietary issues) side chains of the polymer surface can be replaced by atoms or other functional groups just as an anchor.

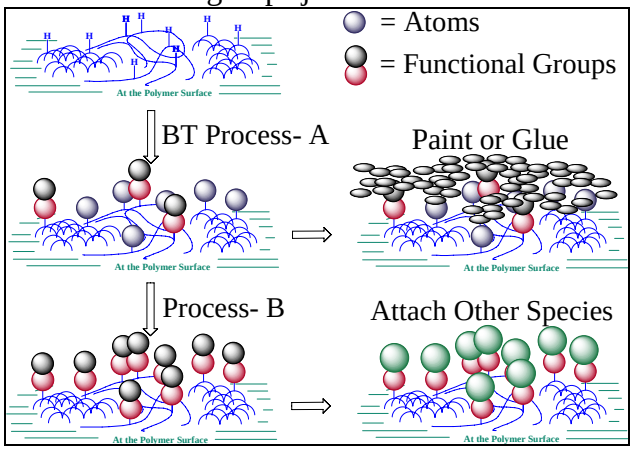

Figure 5: A brief schematic of the patented technology [4-5] used in this study to manufacture the SAS proton exchange membrane.

On the other hand, following the BT process-B side chains of the polymer surface can be modified in order to attach other species (i.e. desired chemical species) onto the polymer backbone. The properties of new SAS PEM were compared with commercially manufactured Nafion® 212. In this study, we compared properties of two SAS membrane, SAS type I and SAS type II with those of Nafion® 212. The difference between the SAS type I and type II are the compositions of monomer ratios (not discussed here due to proprietary issue). The final thickness of both of the SAS membranes reported herein is 50.4 μm which is comparable to the thickness of Nafion® 212 of 50.8 μm.

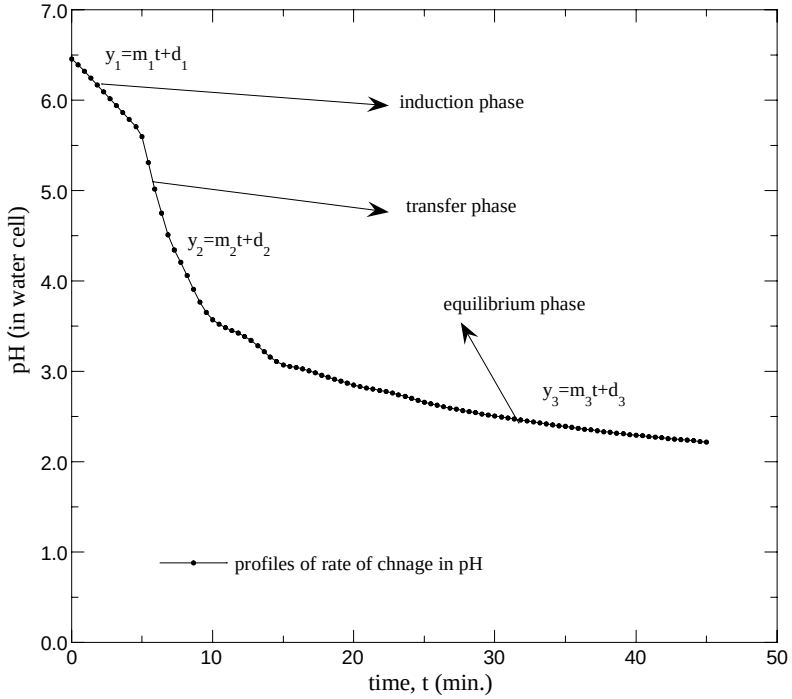

Figure 6: Experimental results for the change of pH in water cell as a function of time with no membrane to determine the rate of diffusion of protons. Linear regression equations at each of the three distinct phases: induction phase, transfer phase and equilibrium phase, are shown in the onset. Slope of the curves indicate the rate of change of pH in each phase.

Figure 6 represents the change of pH in water cell as a function of time without placing membrane between the two cells in order to test diffusion rate of protons (conduction of protons). Figure 6 shows a complete profile of change of pH in the water cell which clearly displays three distinct phases – an *induction phase* representing the time taken for the acid to diffuse into the de-ionized water to release protons up to the moment of time to start transfer of protons from acid cell to water cell i.e. total time taken to gain first proton into the water cell; a *proton transfer phase* wherein protons started passing rapidly into the water cell - lowering the pH of the water cell, and an *equilibrium phase* wherein the pH of the initially water-only cell was lowered approximately to that of the initially acidified cell. Figure 7 represents the change in pH in the water cell at 80^{o}C for different membranes tested here as a function of time. Since the same initial concentration of protons was used for each of the membrane trials, the initial pH was the same for each trial as can be seen from Figure 7. Comparing Figures 6 and 7 revealed the variations in the profiles of proton

concentration in the water cell due to the presence of membrane which leads to quantify proton transfer rate through the membrane.

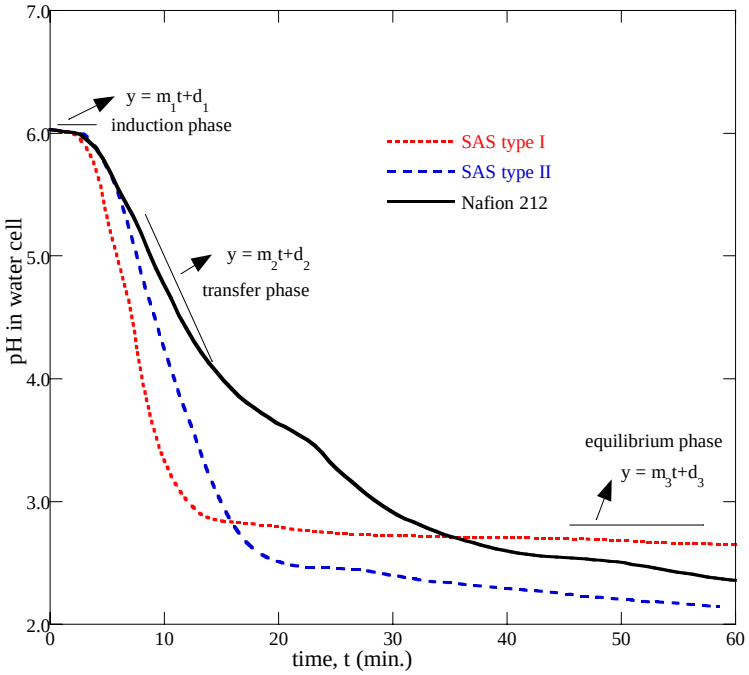

Figure 7: Experimental results for the change of pH in water cell as a function of time with different membranes at 80°C. Linear regression equations at each of the three distinct phases: induction phase, transfer phase and equilibrium phase, are shown in the onset. Slope of the curves indicate the rate of change of pH in each phase.

The profiles of rate of pH change in the water cell (see Figure 7) provided a curve consisting of three segments [6]: an initial slightly negative slope representing an *induction phase*, a greater negative slope – the *transfer phase* and then a final slightly negative slope denotes an *equilibrium phase*. The entire profile of the rate of pH change curve was then separated into three separate curves, one for each region of different slope, and a linear regression line fitted to each curve segment with corresponding linear equations. The induction phase is used to determine the time required for each of the membrane to start transfer proton to the water cell. The *proton transfer phase* was used to determine the concentration of protons (i.e. total amount of protons) transferred into the water cell per minute and the time from initiation of proton transfer into the initially water-only cell till attainment of the equilibrium pH between the two cells. The slope of the middle, strongly negative curve - *protons transfer phase curve*, represents the maximum rate of proton transfer per minute and can be calculated as the "change in negative logarithm of the hydrogen ion (proton) concentration per minute" or Log[H^+]/min. The two intersections of the three curves, shown in Figure 7, were then obtained to provide the onset of protons crossing the membrane and the attainment of pseudo-equilibrium [6]. The slope was then converted to moles of protons to obtain the "change in concentration of protons / minute" and the final protons concentration is multiplied by 6.02×10^{23} (Avogadro number) to obtain the actual number of protons per minute transferred through the membrane in the water cell. The proton concentration thus obtained was then inverted to obtain time required per mole of protons and time required per proton to pass through the membrane, respectively.

Using regression line equations, given in [6],

$$y_1 = m_1 t + d_1, \quad (3)$$

$$y_2 = m_2 t + d_2, \quad (4)$$

and

$$y_3 = m_3 t + d_3, \quad (5)$$

where m_1, m_2, and m_3 represent the rate of pH change in the water cell at each of the three distinct phases; *induction phase*, *transfer phase* and *equilibrium phase*, respectively, the rate of change (slope) of pH profiles for each of the tested membrane at 80°C was then calculated. The rate of change of pH profiles in the water cell, obtained from Figure 7, is presented in Figure 8. In Figure 8, it can be seen that the induction phase provided a steady constant slope while significant slope variations were obtained in the proton transfer phase. Finally, a steady constant slope was again obtained in the equilibrium phase and signaled the attainment of pseudo-equilibrium of proton concentration between the acid cell and the water cell. The slope characteristics of pH profiles in water cell described how the proton conduction is taking place between the two cells.

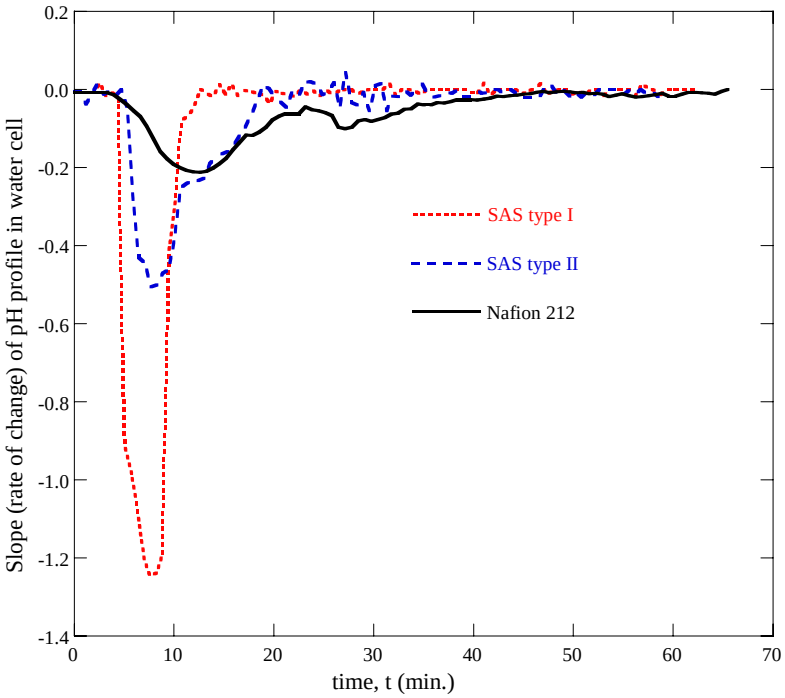

Figure 8: Slopes (rate of change) of pH profiles in water cell as a function of time with different membranes at 80°C. SAS membranes show very sharp decrease of slopes in the transfer phase as compared to Nafion® 212 membrane.

From Figure 8, we can see that the sharp decrease in slopes throughout the transfer phase for both of the SAS membranes as compared to Nafion® 212 membrane. Using the rate of pH change in the water cell in Figure 8 and the relation given in the equation below [6]:

Concentration of protons: $\left[H^+\right]=10^{-pH}$, (6)

we calculated moles of protons transferred through the membrane and obtained the concentration of protons per minute for each of the membranes examined. Figure 9 represents the concentration profiles of proton flow as a function of time in the water cell for various membranes. This was

obtained experimentally by placing the membrane between the two test cells (shown in Figure 4) and the corresponding theoretical results were obtained using the theoretical model, given in equation (1). In this calculation, we used values of C_0 and C_f obtained experimentally through the rate of pH change as shown in Figure 8. In Figure 9, both the experimental results and theoretical results are presented. As can be seen, there is an excellent agreement between the experimental and theoretical profiles of proton flow (see Figure 9) in all of the three phases. The peak of the profiles of proton flow represents the maximum rate of protons transfer. Among the profiles of proton flow for different membranes, SAS type I PEM has the highest peak and Nafion® 212 has the lowest peak. This indicates that the SAS type I PEM is able to transfer more protons per unit time than the Nafion® 212 membrane at 80°C.

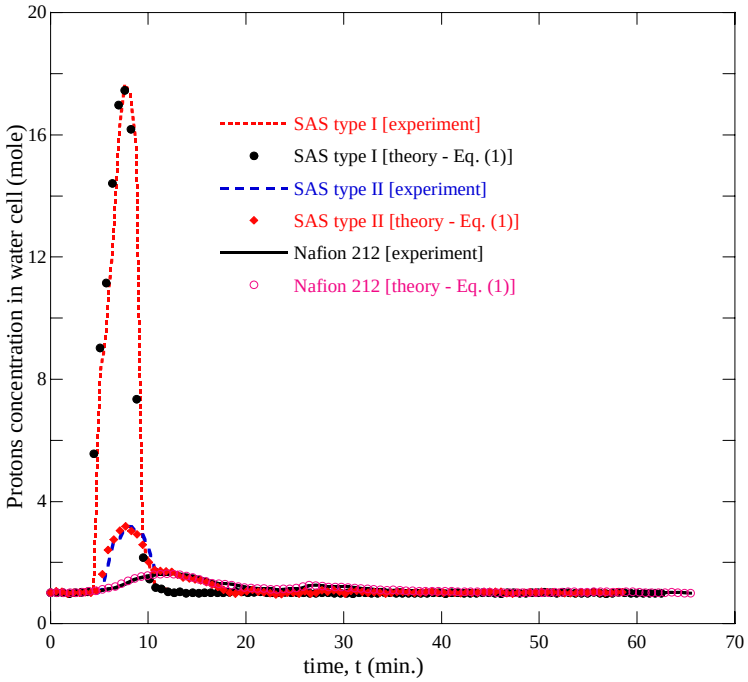

Figure 9: Concentration profiles of protons flow in water cell at 80°C as a function of time for different membranes. Symbols represent experimental results. Solid-, dashed- and dotted-lines represent theoretical model predictions for different membranes.

1.5.1: Membrane conductivity at different temperatures

To determine the stability of the SAS membranes in hydrolytic conditions i.e. fuel cells operating conditions, the membranes were immersed into the water at different temperatures for 24 hours and then their proton transfer capacity tested. The proton transfer capacity for each of the membranes tested here was determined in the range of 25°C to 90°C in order to judge the membrane conductivity at different temperatures. The experimental procedures discussed in section 3 were followed to examine the proton transfer capacity for each of the membranes at different temperatures. This experimental test was done by placing the membrane sandwich between the conductive media as shown in Figure 4. The reported values are the mean of at least five experiments. The standard deviation from the mean values of proton transfer capacity was ±2%. Figure 10 shows the maximum proton transfer capacity for each of the membranes examined. Maximum proton transfer capacity is determined using the highest peak slope shown in Figure 8 at different temperatures examined in this study. From Figure 10, it can be seen that both SAS type

membranes were able to transfer higher number of protons in the temperature range 25°C ~90°C than the Nafion® 212 membrane. The maximum proton transfer rate increases as the temperature increases for all of the membranes. Proton transfer rate through the membranes was almost constant between 25°C~60°C (Figure 10). SAS type membranes started transfer protons rapidly after 60°C compared to Nafion® 212 membrane.

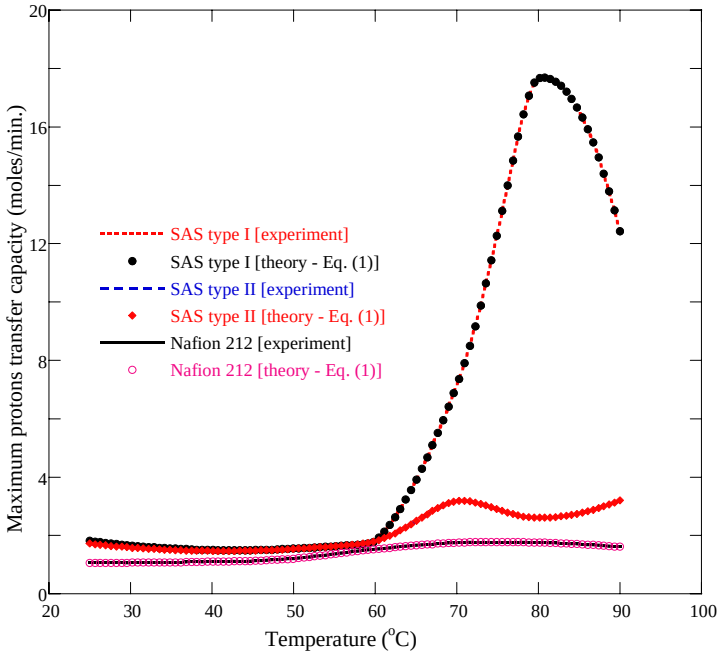

Figure 10: Maximum protons transfer capacity among membranes at different temperatures. Dashed, dotted and solid lines represent experimental results and symbols represent theoretical results [6].

At 80°C, SAS type I membrane provided the highest proton transfer rate, approximately 18 moles per minute, compared to the Nafion® 212 membrane, approximately 1.8 moles per minute. This indicates that this SAS type I membrane had 10 times faster protons transfer capability than the Nafion® 212 membrane at low temperature PEM fuel cells operating conditions i.e. at 80°C. Figure 10 also shows a slow decrease in proton concentration profiles after 80°C for SAS type I membrane as temperature increases. Since the protons present in the water cell are in the form of H_3O^+ and not simply H^+, it is not known immediately what the significance of this shifted trend would be after 80°C especially when considering a hydrogen fuel cell. Thus, further investigation is needed to understand the trend. Figure 11 represents the average proton transfer capacity for each of the membranes examined at different temperatures. Average proton transfer capacity was determined using the average slope calculated using the protons transfer phase profiles in water cell as shown in Figure 7 at 80°C. Following a similar procedure as that used to generate the curves in Figure 8, the average slope in the proton transfer phase in water cell was calculated. Hence, the average change in proton concentration with time (i.e. protons transfer rate) was determined for different temperatures, 25°C~90°C. In Figure 11, dotted, dashed and solid lines represent experimental results and symbols represent theoretical results [6]. Average proton transfer rates of SAS type I membrane was determined to be 10.5 moles per minute, compared to 1.5 moles per minute for Nafion® 212 membrane. This implies that SAS type I membrane has 7 times faster

average proton transfer rate than Nafion® 212 membrane under the test conditions utilized in this study. Figure 12 represents the minimum time required for the protons to pass through the membrane at different temperatures. The minimum time required for each membrane was determined by the difference in time it just started to transfer protons into the water cell and the time it takes to transfer protons at its highest capacity, determined by the peak in the concentration profiles at different temperatures as shown in Figure 9 at 80°C. Comparing results given in Figure 12, suggests that SAS type I membrane took 71% less time at 25°C and 87% less time at 80°C compared to the Nafion® 212 membrane to transfer a mole of protons. Both experimental and theoretical results are presented in Figure 12, where dotted, dashed and solid lines denote experimental and symbols represent theoretical results [6].

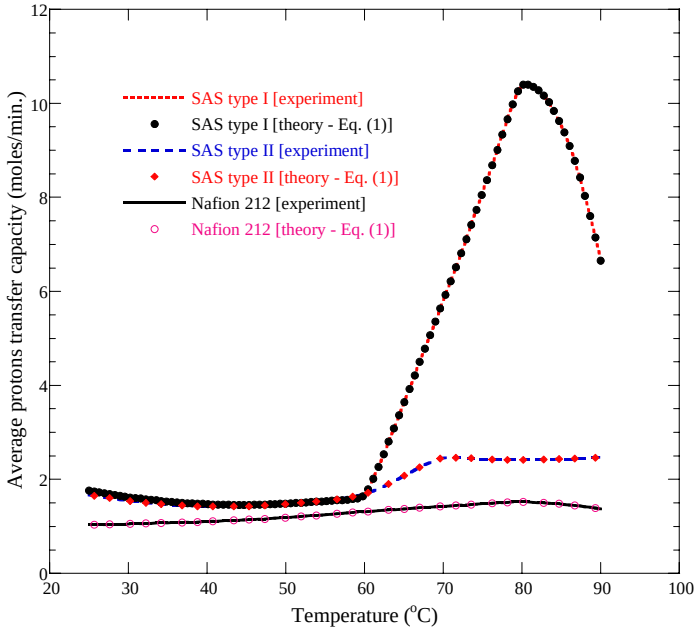

Figure 11: Average protons transfer capacity among membranes at different temperatures. Dashed, dotted and solid lines represent experimental results and symbols represent theoretical results [6].

Both experimental and theoretical results are in good agreement. Figure 13 represents the average time required for one mole of protons to pass through the membrane per minute at different temperatures. Both experimental and theoretical results are presented in Figure 13. The average time was calculated by the initiation and the termination of proton transfer in the transfer phase profiles at different temperatures in the same manner as the curves in Figure 12 were obtained. Both SAS type membranes took less average time to transfer per mole of protons compared to Nafion® 212 membrane. At 25°C SAS type I membrane took 70% less average time whereas at 80°C about 85% less average time than the peer Nafion® 212 membrane. This implies that both SAS type membranes are able to transfer protons at higher rates and at less average time per mole compared to the Nafion® 212 membrane. Figure 14 shows the induction time required for protons to begin passing through the membrane at different temperatures and was calculated using [6]:

$$t_1 = \frac{d_2 - d_1}{m_1 - m_2}. \qquad (7)$$

From Figure 14, it can be determined that at low temperature (i.e. 25°C), Nafion® 212 membrane has a higher induction time compared to SAS type membranes. The induction time decreases with

increasing temperatures. At 80°C, the induction time of Nafion® 212 is 2 times longer than the SAS type I membrane (Figure 14). This indicates that the SAS type I membrane is able to start transferring protons 2 times earlier compared to Nafion® 212 at 80°C.

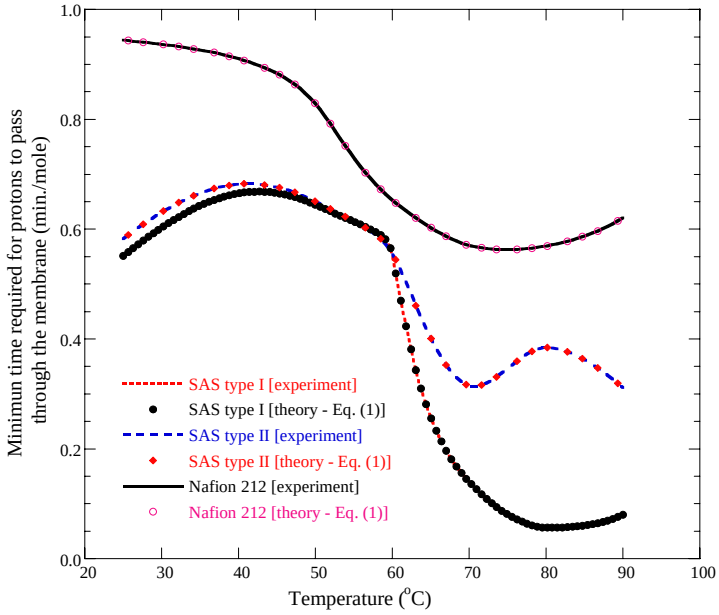

Figure 12: Minimum time required for protons to pass through the membrane at different temperatures. Dotted, dashed and solid lines represent experimental results and symbols represent theoretical results [6].

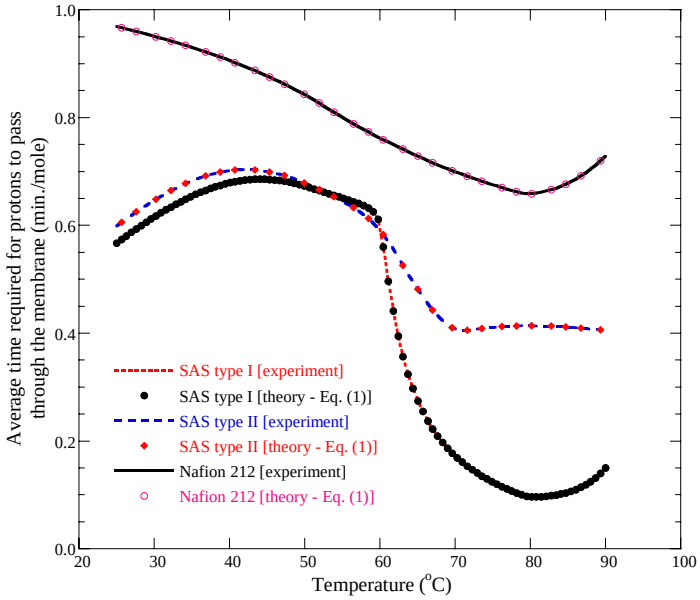

Figure 13: Average time required for protons to pass through the membrane at different temperatures. Dashed, dotted and solid lines represent experimental results and symbols represent theoretical results [6].

1.5.2: Relative Resistance of Membranes

Figure 15 provides the minimum relative resistance between membranes at different temperatures. The theoretical relative resistance was calculated according to the theoretical model [6]. According to the model [6], the membrane's relative resistance is directly proportional to the total time taken by the membrane to allow a specific amount of protons to pass through it.

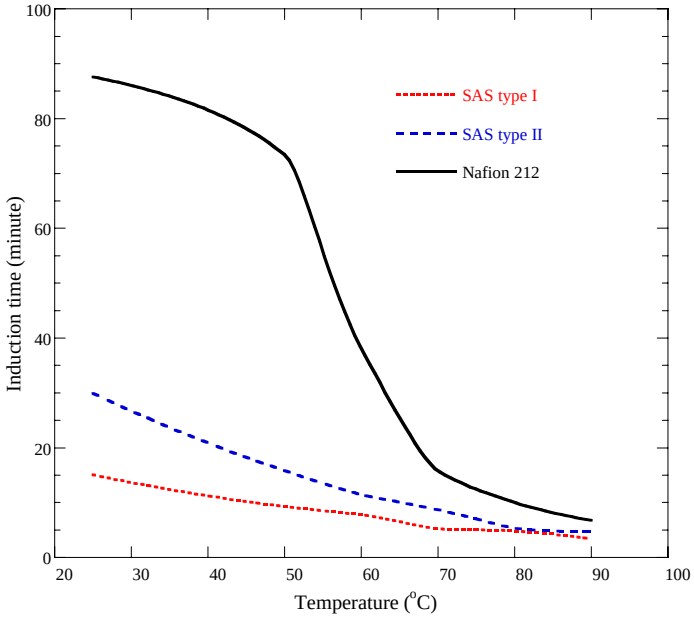

Figure 14: Induction time required for protons to pass through the membrane at different temperatures. Dotted, dashed and solid lines represent results for SAS type I, SAS type II and Nafion® 212 membrane respectively.

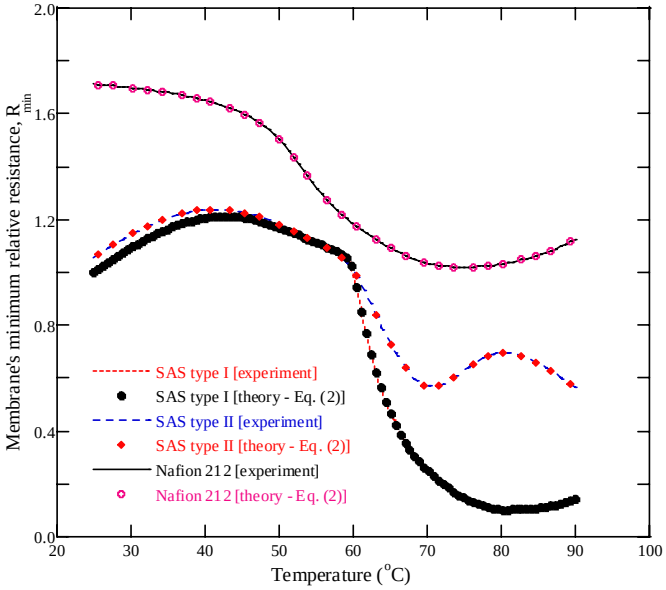

Figure 15: Membrane's minimum relative resistance at different temperatures. Dashed, dotted and solid lines represent experimental and symbols represent theoretical results [6].

Using the concentration profiles of protons in the water cell, as shown in Figure 9 at 80°C, we then evaluated the relative membrane resistance at different temperatures. The minimum

membrane resistance (R_{min}) was calculated from the time it took each membrane to transfer a mole of protons at its peak transfer rate at different temperatures. The results in Figure 15, suggest that the relative resistance for Nafion® 212 is 72% higher than the SAS membrane at 25°C and 87% more at 80°C. Membrane resistance has a great impact on the performance of low temperature proton exchange membrane fuel cell since high membrane resistance causes a drop of fuel cell's overall Ohmic voltage [3].

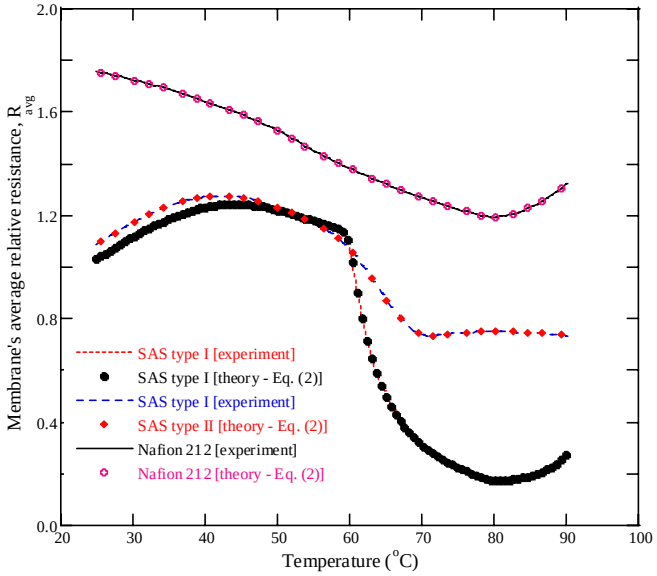

Figure 16: Membrane's average relative resistance at different temperatures. Dashed, dotted and solid lines represent experimental results and symbols represent theoretical results [6].

Among the membranes reported in this study, the SAS type I membrane has the lowest resistance and Nafion® 212 has the highest resistance at all temperatures (Figure 15). The average relative resistance (R_{avg}) of these membranes is presented in Figure 16. Dotted, dashed and solid lines show the experimental and symbols represent the theoretical results [6]. Average relative resistance (R_{avg}) was calculated using the average time each membrane took at different temperatures to transfer protons through the entire transfer phases (seen Figure 7). In Figure 16, it can be seen that the average relative resistance of Nafion® 212 is much higher than the SAS type membranes at different temperatures. At 25°C, average relative resistance of Nafion® 212 membrane is 65% higher and at 80°C the average relative resistance is about 80% higher than the SAS type I membrane. Since low resistance is a requirement for the enhancement of low temperature PEM fuel cells performance, SAS type I membrane shows a promise to perform better than Nafion® 212 membrane.

1.5.3: Water uptake content

The swelling characteristics of the SAS membranes were determined by water uptake measurements. The membrane samples were dried, weighed and soaked in deionized water for 24 hours at temperatures ranging from 25°C to 90°C. The membranes were then blotted dry and further air dried after which they were re-weighed. This procedure was repeated at least five times until a satisfactory reproducibility was obtained. The water uptake content was calculated using the following relationship:

$$\text{water uptake content, } w(\%) = \frac{w_{wet} - w_{dry}}{w_{dry}} \times 100, \tag{8}$$

where w_{dry} and w_{wet} are the weights of the dry and wet membrane samples, respectively. Figure 17 shows the water uptake content of membranes at different temperatures. Dotted, dashed and solid lines represent the SAS type I, SAS type II and Nafion® 212 membrane respectively.

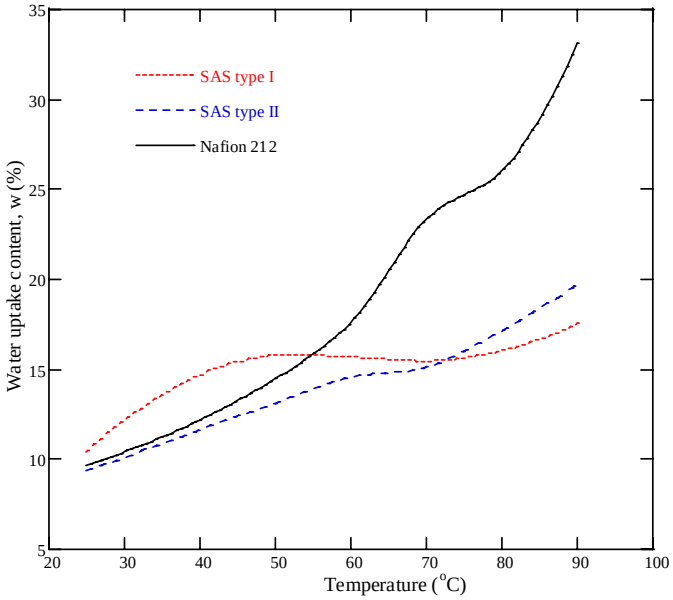

Figure 17: Membrane's water uptake content at different temperatures. Dotted, dashed and solid lines represent SAS type I, SAS type II and Nafion® 212 membrane respectively.

From Figure 17, we see that the water uptake content for Nafion® 212 membrane is very high and increased almost linearly with increasing temperature as compared to SAS type membranes. This implies that to conduct proton transfer efficiently, Nafion® 212 requires more water (i.e. higher humidity level) than the SAS type membranes. It appears that SAS type membranes are capable of transferring protons efficiently at low water content than Nafion® 212 as well. The dependence of the liquid water uptake could have significant implications for the use of membrane in PEMFCs [52]. For example, in one common mode of fabrication of membrane-electrode assemblies (MEAs), the membrane and electrodes are hot-pressed together at higher temperature (e. g. at 120°C). During this process, all water is lost from the membrane and the operational temperature to which the membrane is exposed (e.g. 80°C) could result in incomplete rehydration. If less water is taken up by the membrane, a decrease in the maximum attainable conductivity would occur since the conductivity depends strongly on membrane water content and hence on membrane's relative humidity. In general, it is assumed that the membrane will regain the required hydration level once soaked into the water prior to use in the fuel cell environment. A rigorous relative humidity (RH) cycle measurement is studied using industry-standard test protocols (BekkTech) to verify the performance of these membranes in terms of conductivity, resistance, temperature, relative humidity and other parametric conditions.

1.6: SAS membrane performance evaluation using industry-standard test protocols

We validated membrane performance both at the laboratory scale and using industry-standard testing protocols. We sent our membrane samples to the BekkTech testing service, an industry-standard membrane sample testing service provider, and obtained preliminary results regarding the membrane conductivity, resistivity, thickness measurements and relative humidity (RH) cycling at 30°C, 80°C and 120°C for batch 1 and batch 2 membrane sample.

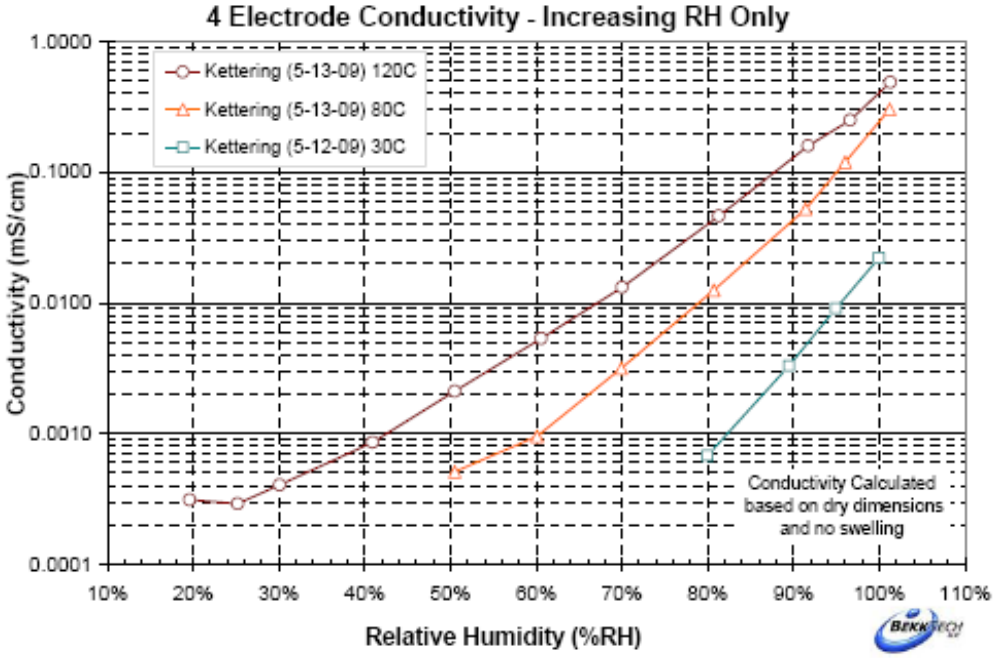

(a)

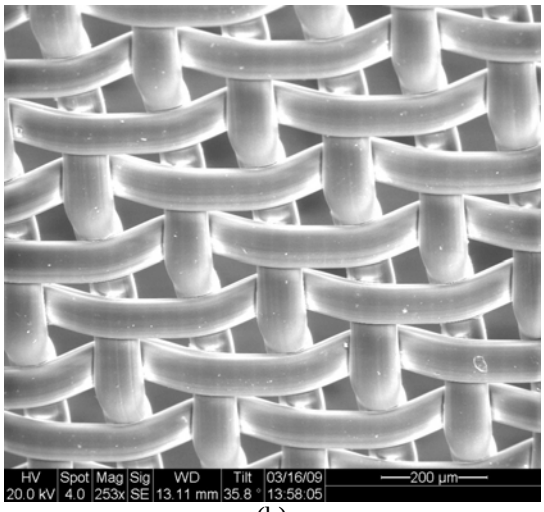

(b)

Figure 18. (a) 4-electrode conductivity test of our developed SAS-type membrane (batch 1 sample – SAS type I) with different relative humidity at 30°C, 80°C and 120°C. (b) SEM image of SAS (***s***tyrene-***a***crylic acid-vinyl***s***ulfonate) membrane – produced at Kettering facility.

Figure 18a represents the 4-electrode conductivity measurement in different relative humidity at 30°C, 80°C and 120°C. From Figure 18a, we can see that our SAS-PEM membrane (batch 1 sample – SAS type I) is able to conduct proton at different RH levels but required further improvement in terms of proton conductivity at a reduced humidity conditions. Figure 1b represents the SEM image of our PEM membrane which shows the presence of proton conductive media onto the inert mesh we used for mechanical and chemical stability of the membrane. After

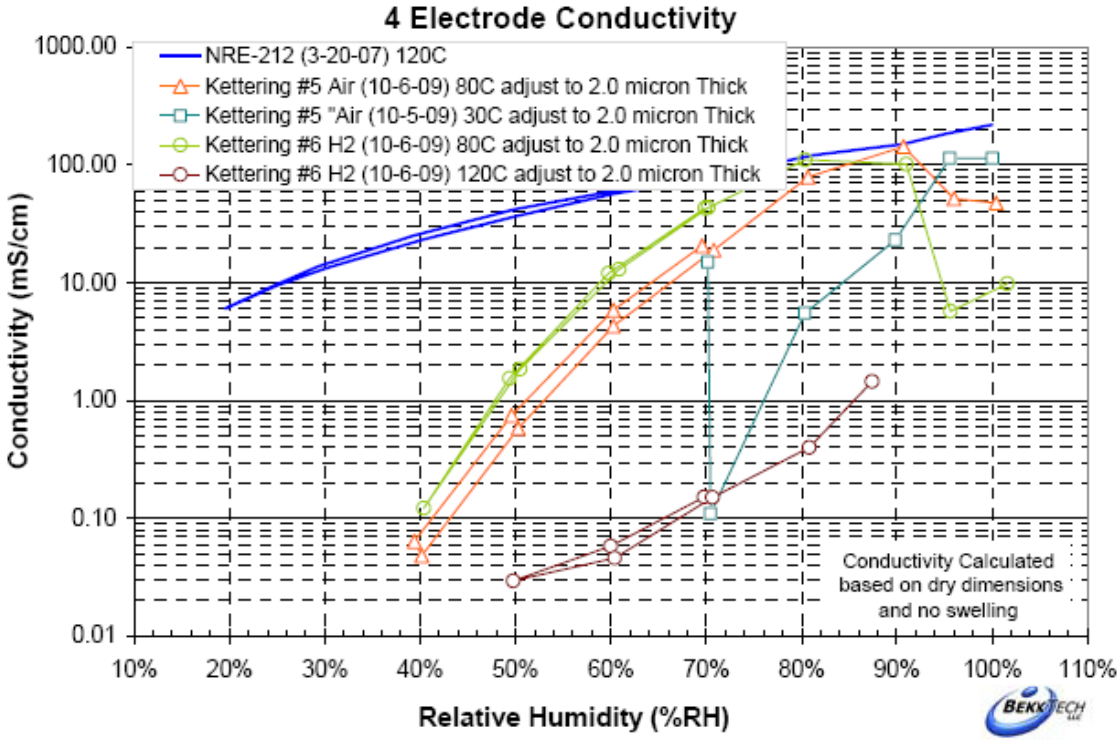

Figure 19: 4-electrode conductivity test of our developed SAS-type membrane (batch 2 sample – SAS type I) with different relative humidity at 30°C, 80°C and 120°C.

analyzing our SAS membrane (batch 1 sample) performance, evaluated using industry-stand protocols, we refined our sample preparation mesh and prepared batch 2 sample. Batch 2 sample test results by BekkTech are presented in Figure 19. Comparing results in Figure 18a and 19 we found that the conductivity of our membrane sample improved significantly, from 2 mS to 100mS at 80%-90% RH cycling. Batch 2 membrane sample performance is well comparable with the commercial membrane Nafion 212 but fell far below our laboratory test results presented in Figures 7 to 11. At this stage we were run-out of fund (DOE grant expired with no additional funding) to prepare any additional sample to test using industry-standard protocols. We are putting efforts forward to obtain fund from other external funding sources in order to continue preparation of refined membrane sample to achieved industry-standard test results close to our laboratory based test results. Our future efforts will mainly be directed towards preparation of membrane samples in order to accommodate performance enhancement required in the operational PEM fuel cell environment.

1.7: Conclusions (PEM membrane development)

The purpose of the research reported here is the development of a complete manufacturing procedure to fabricate a novel PEM, for fuel cell applications, that has the potential to be more efficient, robust and less expensive than Nafion®. The objectives of improved proton conductivity through a proton exchanging polymer matrix cast onto a very mechanically and chemically stable robust ETFE mesh were achieved by separating different PEM requirements and distributing them among different PEM polymer matrices. In the present study, many of the structural and mechanical requirements were met by the ETFE mesh while the proton exchange polymer media was designed to optimize proton transfer capacity. Although the materials used to prepare these hybrid membranes were purchased from specialty chemical and polymer companies, the cost of ETFE used in the current study was approximately \$353 m^{-2} and that of the chemicals was under \$20.00 m^{-2}. Manufacturing costs are also relatively low and the preparation and casting of the membrane cocktail onto the mesh did not require any expensive special equipment. It is thus anticipated that larger scale manufacturing of SAS type PEMs will be significantly less expensive than the manufacture of Nafion®-type membranes. The results of the current study also indicate that the hybrid SAS type proton exchange polymer matrix may be tailored to meet a range of low temperature fuel cells requirements. In this study, we have shown that the basic requirements such as proton exchange capacities, relative resistance, temperature variations effect, induction time and water uptake content are significantly improved in SAS type membranes especially SAS type I membrane as compared to Nafion® 212 membrane. A detailed experimental set-up to validate the performance with the theoretical model has also been developed and described. The results also show that the theoretical model predictions are in an excellent agreement with the experimental observations. The two samples of our SAS-type membrane (batch 1 and Batch 2) tested using industry-standard test protocols show significant improvement of membrane conductivity at different RH cycling and the performance is comparable with the commercial membrane Nafion 212. The laboratory-based results reported here for the new SAS type PEMs is promising (see Figures 8-11). Although all the DOE project requirements are met at least at the laboratory-based test level but further characterization of new SAS type PEM using industry-standard commercial equipments will be done in future (with more refined sample) subject to availability of external funds.

2. **Development of multiphase CFD flow model for PEM fuel cell**

2.1 Abstract:

To understand heat and water management phenomena better within an operational proton exchange membrane fuel cell's (PEMFC) conditions, a three-dimensional, two-phase flow model has been developed and simulated for a complete PEMFC. Both liquid and gas phases are considered in the model by taking into account the gas flow, diffusion, charge transfer, change of phase, electro-osmosis, and electrochemical reactions to understand the overall dynamic behaviors of species within an operating PEMFC. The model is solved numerically under different parametric conditions in terms of water management issues in order to improve cell performance. In this study, mostly cathode side results of a complete PEMFC are presented. The results obtained from two-phase flow model simulations show improvement in cell performance as well as water management under PEMFCs operational conditions as compared to the results of a single phase flow model available in the literature. The quantitative information obtained from the two-phase model simulation results will help to open up a route in designing improvement of PEMFC for better operational efficiency and performance.

2.2: Model Description:

The multiphase CFD flow model developed here primarily based on the multiphase approach of Abriola and Pinder [9] and the mixture multiphase flow model of Wang and Chen [10]. We used the two-phase flow model in both the anode catalyst layer and cathode catalyst layer as well as in the two gas channels included in the unified modeling domains shown in Figure 1. In addition, mass and momentum transfer between the liquid and gas phases due to phase change is taken into consideration. Distinct from previous model, the present model considers the anode feed consisting of hydrogen and water vapor, whereas humidified air is fed into the cathode channel as related to the real world experiment/operation of proton exchange membrane fuel cell (PEMFC). Hydrogen oxidation and oxygen reduction reactions are considered to occur only within the active catalyst layers where Pt/C catalysts are intermixed uniformly with recast ionomer. In the schematic of unified modeling domains of a unit fuel cell shown in Figure 20, three different domains (seven subregions in total) are considered, one for the anode fluid, one for the cathode fluid, and one for the water. The anode and cathode domains each consists of the respective gas channel, gas diffusion layer (GDL) and the catalyst layer (CL), and the domain for water - include all the components: two gas channels, two GDLs, two catalyst layers and the membrane.

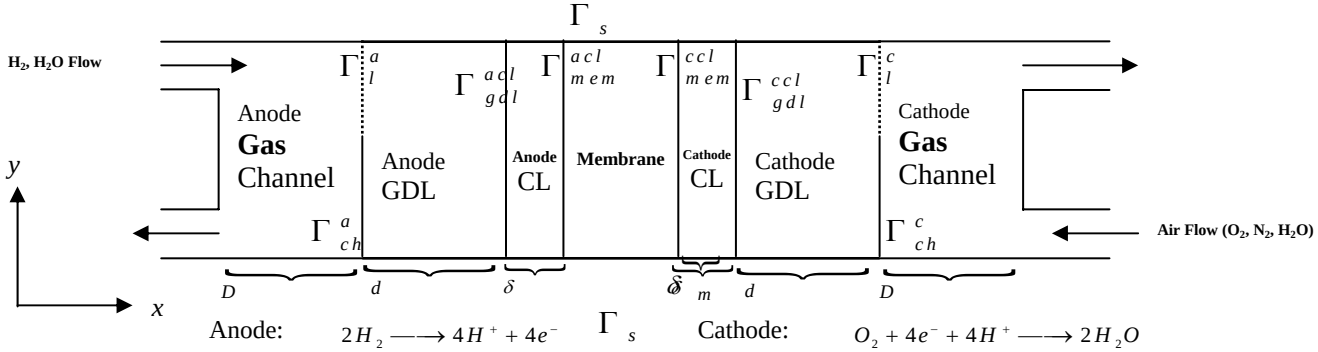

Figure 20: Schematic of unified modeling domains of a unit PEM fuel cell. *D* is the channel depth; *d* is the gas diffuser thickness; δ is the catalyst layer thickness; and δ_m is the membrane thickness.

x and y denotes the direction of 2D geometry. Arrow sign represents gas flow direction and $\Gamma^{'s}$ shows various boundary conditions within the unified modeling domains.

2.3: Key assumptions

The following assumptions are made in the model development: (i) ideal gas mixtures, (ii) the flow is incompressible, unsteady and laminar everywhere due to small pressure gradients and flow velocities, and (iii) the gas diffusers; catalyst layers and membrane each are considered as non-deformable isotropic porous media. However, since the gas diffuser is very thin and the velocity gradient is very high at its interface with the gas channel, the macroscopic inertial force and viscous force cannot be neglected.

2.4: Model governing equations

At any point (location) in the gas diffuser and the gas channel, the total mass of the two-phase mixture is conserved [10]:

$$\varepsilon \frac{\partial \rho}{\partial t} + \nabla \cdot (\rho \mathbf{u}) = 0 \tag{9}$$

where ε is the porosity and it equals 1 in the channels if the liquid volume fraction is zero. **u** is the velocity vector, *t* is the time, and ρ is the density. The Navier-Stokes equation is applied for the two-phase mixture in the gas channel:

$$\frac{1}{\varepsilon}\left[\frac{\partial(\rho \mathbf{u})}{\partial t} + \frac{1}{\varepsilon}\nabla \cdot (\rho \mathbf{u}\mathbf{u})\right] = -\nabla p + \nabla \cdot (\mu \nabla \mathbf{u}) \tag{10}$$

where *p* stands for pressure and μ denotes viscosity.

A generalized Darcy law [11] is more suitable for describing the momentum conservation of two-phase mixture flow in the gas diffuser:

$$\frac{1}{\varepsilon}\left[\frac{\partial(\rho \mathbf{u})}{\partial t} + \frac{1}{\varepsilon}\nabla \cdot (\rho \mathbf{u}\mathbf{u})\right] = -\nabla p + \nabla \cdot (\mu \nabla \mathbf{u}) - \frac{\mu}{K}(\mathbf{u}) \tag{11}$$

where *K* stands for absolute permeability and the last term on right hand side represents the drag of the porous solid on the liquid [12]. Note that the interfacial shear force and surface tension gradient force between the liquid phase and the gas phase cancelled out and thus do not appear in Equations (10) and (11). It can be seen that the Equation (10) is a special form of the general Equation (11) and can be solved together in the coupled domain shown in Figure 20. As shown in Figure 20, the humidified air/hydrogen flows in a heterogeneous domain that includes a homogeneous fluid and a porous medium. If the governing equations are written separately in the fluid channel and gas diffuser, the boundary conditions at the gas channel/gas diffuser interface are difficult to specify, and a considerable effort is needed to couple the flow and transport of both regions. Since the velocity, pressure and species mass fractions are continuous at the gas channel/gas diffuser interface, a unified approach is applied [13]. The unified approach solves the governing equations in the gas channel and gas diffuser simultaneously, so the necessity to specify the interface boundary conditions is avoided.

The general species conservation equation for the multi-phase mixture in gas diffuser is given by [10]:

$$\varepsilon\frac{\partial}{\partial t}\left(\rho C^{\alpha}\right)+\nabla\cdot\left(\gamma_{\alpha}\rho\mathbf{u}C^{\alpha}\right)=\nabla\cdot\left(\varepsilon\rho D^{\alpha}\nabla C^{\alpha}\right)+$$
$$\nabla\cdot\left[\varepsilon\sum_{k}\left\{\rho_k s_k D_k^{\alpha}\left(\nabla C_k^{\alpha}-\nabla C^{\alpha}\right)\right\}\right]-\nabla\cdot\left[\sum_{k}C_k^{\alpha}\mathbf{j}_k\right] \quad (12)$$

Here C represents concentration of species, D is the diffusion constant, and s is the phase saturation. The first two terms on the right hand side of Equation (12) combine represent the net Fickian diffusion flux within various phases, while the last term on the right hand side represents the diffusive flux across the phases. The second term on the left hand side of Equation (12) indicates that species α is advected, on the mixture level, by a modified velocity field $\gamma_{\alpha}\mathbf{u}$ rather than the original mixture velocity field where γ_{α} is called a correction factor for species advection and is defined as:

$$\gamma_{\alpha}=\frac{\rho\sum_{k}\lambda_k C_k^{\alpha}}{\sum_{k}\rho_k s_k C_k^{\alpha}} \quad (13)$$

Since we are dealing with a two-phase flow problem, thus $k=2$ (liquid (l) and gas (g) phases); α denotes species which includes hydrogen, oxygen, nitrogen and water. Similar to the classical multi-component mixture, a multiphase mixture can be considered as a fluid consisting of diffusing constituents (phases). As a result, the mixture density and velocity can be defined, respectively, as:

$$\rho=\sum_{k}\rho_k s_k=\rho_l s_l+\rho_g s_g;\ \ k=l,g \quad (14)$$

$$\rho\mathbf{u}=\sum_{k}\rho_k\mathbf{u}_k=\rho_l\mathbf{u}_l+\rho_g\mathbf{u}_g \quad (15)$$

Noting that the superficial velocity of a phase, $\mathbf{u}_k$, is related to its intrinsic velocity by the phase volume fraction. Therefore Equation (15) implies that the mixture velocity is a mass-weighted average of the intrinsic phase velocities. The mixture kinematic viscosity is given by

$$\nu=\left(\sum_{k}\frac{k_{rk}}{\nu_k}\right)^{-1} \quad (16)$$

and the mobility of each phase in the multiphase mixture is defined as

$$\lambda_k=\frac{k_{rk}}{\nu_k}\nu;\ \ \sum_{k}\lambda_k=1 \quad (17)$$

The mass-averaged mixture concentration of species α over all phases is defined as

$$\rho C^{\alpha}=\sum_{k}\rho_k s_k C_k^{\alpha}=\rho_l s_l C_l^{\alpha}+\rho_g s_g C_g^{\alpha}\ \text{ for two-phase case} \quad (18)$$

and the effective diffusion coefficient for the multiphase mixture is defined as

$$\rho D^{\alpha}=\sum_{k}\rho_k s_k D_k^{\alpha}=\rho_l s_l D_l^{\alpha}+\rho_g s_g D_g^{\alpha}\ \text{ for two-phase case} \quad (19)$$

The advection correction factor, λ_{α}, defined in Equation (13), for our two-phase problem, becomes

$$\lambda_{\alpha}=\frac{\rho\left[\lambda_l C_l^{\alpha}+\lambda_g C_g^{\alpha}\right]}{\rho_l s_l C_l^{\alpha}+\rho_g s_g C_g^{\alpha}};\ \ k=l,g \quad (20)$$

where the individual mobility given in Equations (16)-(17) are

$$\lambda_l = \frac{k_{rl}/\nu_l}{k_{rl}/\nu_l + k_{rg}/\nu_g} \tag{21}$$

$$\lambda_g = \frac{k_{rg}/\nu_g}{k_{rl}/\nu_l + k_{rg}/\nu_g} \tag{22}$$

and

$$\nu = \frac{1}{\left(k_{rl}/\nu_l\right) + \left(k_{rg}/\nu_g\right)}. \tag{23}$$

The relative permeabilities for the liquid and gas phases are represented by the following empirical correlation [13]:

$$k_{rl} = s_l^3; \quad k_{rg} = \left(1 - s_l\right)^3 \tag{24}$$

Now for diffusive mass flux term, $\mathbf{j}_k$, appeared in Equation (12), we will apply the rule of mixture theory. Thus, a diffusive mass flux of phase *k* within the two-phase mixture can be defined as:

$$\mathbf{j}_k = \rho_k \mathbf{u}_k - \lambda_k \rho \mathbf{u} \tag{25}$$

$$\sum_k \mathbf{j}_k = 0 \;\Rightarrow\; \mathbf{j}_l + \mathbf{j}_g = 0 \tag{26}$$

$\mathbf{j}_l$ can be expressed as

$$\mathbf{j}_l = k\frac{\lambda_l}{\nu}\left(\nabla p - \nabla p_l\right) = k\frac{\lambda_l \lambda_g}{\nu}\nabla p_c \tag{27}$$

Once $\mathbf{j}_l$ and $\mathbf{j}_g$ are determined, the individual phase velocities can be obtained from the mixture flow field by the following algebraic relations:

$$\rho_g \mathbf{u}_g = \mathbf{j}_g + \lambda_g \rho \mathbf{u}, \tag{28}$$

$$\rho_l \mathbf{u}_l = -\mathbf{j}_g + \lambda_l \rho \mathbf{u}. \tag{29}$$

We assumed that hydrogen, oxygen and nitrogen can't dissolve in liquid water due to their low solubilities, we get:

$$C_l^{H_2} = 0; \;\; C_l^{O_2} = 0; \;\; C_l^{N_2} = 0; \;\; C_l^{H_2O} = 1 \tag{30}$$

Thus we obtain, the water mass concentration fraction in the anode side can be obtained by

$$C^{H_2O} = 1 - C^{H_2} \tag{31}$$

The water mass concentration fraction in the cathode side can be obtained by

$$C^{H_2O} = 1 - C^{O_2} - C^{N_2} \tag{32}$$

The vapor condenses when the vapor partial pressure exceeds the corresponding saturation vapor pressure [14] at the local temperature

$$\log_{10} P_v = -2.1794 + 0.02953T - 9.1837\times10^{-5}T^2 + 1.4454\times10^{-7}T^3 \tag{33}$$

The corresponding vapor density is

$$\rho_v^{H_2O} = \frac{P_v M}{RT} \tag{34}$$

where *M* is the molecular weight, *R* is gas constant and *T* is the temperature. The concentration of water vapor in the gas mixture

$$C_g^{H_2O} = \frac{\rho_v^{H_2O}}{\rho_g} \tag{35}$$

The gas mixture density is

$$\rho_g = \frac{PM_g}{RT} \tag{36}$$

The two-phase mixture density is

$$\rho = \rho_g s_g + \rho_l s_l \tag{37}$$

where the liquid and gas phase saturations denote the volumetric fraction of the void space occupied by individual phases and are given, respectively, as

$$s_l = \frac{\rho C^{H_2O} - \rho_g C_g^{H_2O}}{\rho_l - \rho_g C_g^{H_2O}} \tag{38}$$

$$s_g = 1 - s_l \tag{39}$$

2.5: Pressure correction

The capillary pressure is assumed to be a function of saturation, the general empirical model is

$$p_c = p_g - p_l = \sigma \left(\frac{\varepsilon}{k} \right)^{1/2} J\left(s_l\right) \tag{40}$$

where $J\left(s_1\right)$ is the Leverett function, given by [15]:

$$J\left(s_l\right) = 1.417\left(1-s_l\right) - 2.120\left(1-s_l\right)^2 + 1.263\left(1-s_l\right)^3 \tag{41}$$

where σ is the surface tension. Then

$$\nabla p_c = \sigma \left(\frac{\varepsilon}{k} \right)^{1/2} J'\left(s_l\right) \nabla s_l + \left(\frac{\varepsilon}{k} \right)^{1/2} J\left(s_l\right) \left[\sum_\alpha \frac{\partial \sigma}{\partial C^\alpha} + \frac{\partial \sigma}{\partial T} \nabla T \right] \tag{42}$$

2.6: Transport through membrane

A generalized expression for species transport in the moderately dilute solution (electrolyte) is given by [14]:

$$N_i = -\frac{z_i D_i F C_i \nabla \phi_m}{RT} - D_i \nabla C_i - D_i C_i \nabla \ln\left(a_{i,n}\right) + C_i \mathbf{u} \tag{43}$$

where the first term on the right hand side is zero since water is not charged, the second term is the diffusion term, the third term takes into account non-ideal solution behavior, which is neglected here for simplicity, and the last term represents the net transport due to bulk flow. The net water flux through the membrane is the sum of these water fluxes and the flow induced by the electro-osmotic-drag. Thus we get

$$N_w^{net} = n_d \frac{I}{F} - D_w \nabla C_w - C_w \frac{k_m}{\mu} \nabla P_w \tag{44}$$

where the electro-osmotic-drag coefficient, n_d, is expressed by the following equation [14]:

$$n_d = \frac{2.5}{22} \lambda \tag{45}$$

the water mole concentration, C_w, in the membrane has the form [4]

$$C_w = \lambda c_f \tag{46}$$

and the water diffusion coefficient, D_w, in the membrane can be expressed by the following equation [14]:

$$D_w \equiv n_d 5.5\times10^{-11}\exp\left[2416\left(\frac{1}{303}-\frac{1}{T}\right)\right] \tag{47}$$

Substituting Equations (45) and (46) into Equation (44), we obtain

$$N_w^{net} = 0.1136\lambda\frac{I}{F} - D_w c_f \nabla\lambda - \lambda c_f \frac{k_m}{\mu}\nabla P_w \tag{48}$$

where c_f means the fixed charge concentration in the membrane, and λ stands for the membrane water content $\left[\text{mol } H_2O/\text{equivalent } SO_3^{-1}\right]$. The water content, λ, can be expressed as [14]:

$$\lambda = 0.043+17.81a-39.85a^2+36.0a^3 \quad (0<a\le1) \tag{49}$$

$$\lambda = 14.0+1.4(a-1) \quad (1<a\le3) \tag{50}$$

$$\lambda = 16.8 \quad (a\ge3) \tag{51}$$

where a being the water vapor activity given by

$$a = \frac{x_w P}{P_w^{sat}} \tag{52}$$

where x_w is the mole fraction of water.

2.7: Potential balance

Phase potential balances in the fuel cell are also solved with the continuity relationship.

$$\nabla\cdot\left(\sigma_e^{eff}\nabla\Phi_e\right) = -\nabla\cdot\left(\sigma_s^{eff}\nabla\Phi_s\right) = j_a \text{ for anode} \tag{53}$$

$$\nabla\cdot\left(\sigma_e^{eff}\nabla\Phi_e\right) = -\nabla\cdot\left(\sigma_s^{eff}\nabla\Phi_s\right) = j_c \text{ for cathode} \tag{54}$$

$$\nabla\cdot\left(\sigma_m^{eff}\nabla\Phi_m\right) = 0 \text{ for membrane} \tag{55}$$

where σ_e^{eff} is the effective conductivity, Φ_e and Φ_s are the potential in the electrode, σ_m^{eff} is the effective membrane conductivity, Φ_m is the potential in the membrane, j_a, and j_c, are the transfer current densities at anode and cathode, respectively, for the electrochemical reaction rate, can be expressed by Butler-Volmer equation based on the facts that the anode exhibits fast electrokinetics and hence a low surface overpotential, and that the cathode has relatively slow electrokinetics:

$$j_a = Aj_{0,a}^{ref}\left(\frac{C^{H_2}}{C_{H_2}^{ref}}\right)^{1/2}\left[\exp\left(\frac{\alpha_a F\eta}{RT}\right)-\exp\left(-\frac{\alpha_c F\eta}{RT}\right)\right] \tag{56}$$

$$j_c = Aj_{0,c}^{ref}\left(\frac{C^{O_2}}{C_{O_2}^{ref}}\right)^{1/2}\left[\exp\left(\frac{\alpha_a F\eta}{RT}\right)-\exp\left(-\frac{\alpha_c F\eta}{RT}\right)\right] \tag{57}$$

where A is the catalyst surface area per unit volume, $j_{0,a}^{ref}$ and $j_{0,c}^{ref}$ are reference exchange current densities at anode and cathode respectively, α_a and α_c are the charge transfer coefficient at anode and cathode respectively, and $\eta(x,y)$ is the surface overpotential defined as:

$$\eta(x,y) = \Phi_s - \Phi_e - V_{oc} \tag{58}$$

where Φ_s and Φ_e stand for the potentials of the electronically conductive solid and electrolyte, respectively, at the electrode/electrolyte interface. V_{oc} is the reference open-circuit potential of an electrode.

2.8: Boundary and initial conditions

In order to make the model problem well-posed, appropriate boundary and initial conditions are required for the present multiphase mixture formulation. Boundary conditions are shown in Figure 1. Initial conditions are usually known or taken from a steady-state solution. The inlet molar concentrations are determined by the inlet pressure and humidity according to the ideal gas law. The gas-phase mole fractions are set equal to the inlet conditions and the liquid water saturation is set to zero. At $\Gamma_{ch}^{a}:\ \mathbf{u}=\mathbf{u}_{in}^{a},\ C_k^{\alpha}=C_k^{\alpha,in},\ p=p_k^{a}$, Relative humidity, $RH=RH^{a}$. At $\Gamma_{l}^{a}:\ \Phi_e=0$; at $\Gamma_{l}^{c}:\ \Phi_e=V_{cell}$ (voltage condition i.e. $\Phi_e=-dV$); at $\Gamma_{ch}^{c}:\ \mathbf{u}=\mathbf{u}_{in}^{c},\ C_k^{\alpha}=C_k^{\alpha,in},\ p=p_k^{c}, RH=RH^{c}$. At Γ^{s}: no flux or symmetry condition is applied. Fully developed or no-flux conditions are applied at Γ_{mem}^{acl} or Γ_{mem}^{ccl}: $\frac{\partial \mathbf{u}}{\partial n}=0,\ \frac{\partial C_k^{\alpha}}{\partial n}=0,\ \frac{\partial p}{\partial n}=0,\ \frac{\partial \Phi_e}{\partial n}=0.$ No-slip and impermeable velocity condition and no-flux conditions are applied at the wall:

$$\mathbf{u}=0,\ \frac{\partial C_k^{\alpha}}{\partial n}=0,\ \frac{\partial p}{\partial n}=0,\ \frac{\partial \Phi_e}{\partial n}=0. \tag{59}$$

The fuel and oxidant streams are fully humidified at the cell operating temperature (80^{o}C) and pressures for both anode and cathode. The pressure of the fuel and oxidant streams are set at the GDL and channel boundaries to the anode and cathode operating pressures times the mole fraction of components. The partial pressures of water at the anode and cathode boundaries are calculated from [16]:

$$p_{sat}=\exp\left[\begin{array}{l}73.648-\dfrac{7258.2}{T}-7.3037\log T\\ +\ 4.1653\times10^{-6}T^{2}\end{array}\right] \tag{60}$$

and are divided by the operating pressure to obtain the mole fraction of water.

2.9: Results and Discussions (multiphase CFD flow model)

This study illustrates the implementation of two-phase flow model in the design of a proton exchange membrane fuel cell (PEMFC) cathode. Computational domain is shown in Figure 21. The model is solved by finite element discretization with mesh size of $75\times75\times75$ and found the solutions are independent of meshing. The geometrical, physical and operating parameters are given in Table 2. The specific purpose of the model is to understand the flow phenomena and liquid phase (water) transport. The model domain consists of a unit cell of the cathode where the gas channel is configured in a serpentine shape (see Figure 21). The active layer is modeled as the bottom boundary of the domain. Thus the model neglects current-distribution effects along the thickness of the catalyst layer. In the gas channel section, we model fluid flow in combination with diffusion and convective transport. The plate-shaped subdomain at the bottom represents the porous diffusion layer of the PEMFC cathode. The bottom boundary is the active catalyst layer where the reaction takes place. The electrode reaction in the active layer couples the concentration of oxygen to the electrical current density. The electrode reaction is treated as a boundary condition at the cathode's bottom surface.

Figure 22 shows the composition of the gas in the porous electrode and in the channel. From Figure 22, we see that the high current density results in substantial oxygen depletion in the regions far away from the gas channel. The oxygen weight fraction reaches values as low as 0.03 in the corner to the left in the Figure. There is also a substantial decrease in oxygen weight fraction along the gas channel from inlet to outlet, from 0.145 to approximately 0.1. This solution is based on applying a pressure drop of 25 Pa between the inlet and outlet. In designing the cathode, it is important to exploit the expensive catalyst layer to its maximum efficiency.

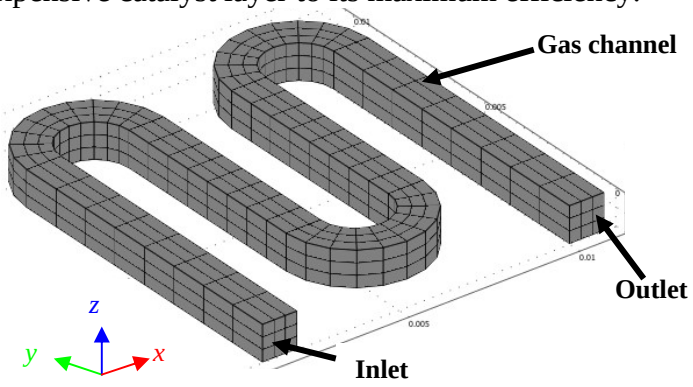

Figure 21: Computational geometry of a serpentine PEM fuel cell cathode. Gas flows through the curved serpentine channels, which sit flush against the cathode layer. Surrounding the channels is the current collector. The bottom boundary of the cathode layer is the catalytic active layer.

Table 2. Geometrical, Physical and operating parameters

Quantity	Value
Gas channel depth/width	0.5/1.0mm
GDL thickness	0.2mm
Catalyst layer thickness	0.01 mm
Membrane thickness	0.020mm
Anode/Cathode pressure	2.0/2.0 atm
Stoichiometry fuel/air @ 1.0A/cm^2	125/200
Porosity of GDL/catalyst layer	0.5/0.3
Thermal conductivity of membrane	0.9W/m K
Thermal conductivity of GDL/catalyst layer	3.0/3.0w/mK
Viscosity of liquid water	2e^{-5} kg/m s
Contact angle	110^o
Permeability of GDL	10^{-11}m^2
Cell temperature	80^{o}C
Exchange current density	1.0
Faraday constant	96487
Surface tension, liquid-water-air @ 80^{o}C	0.0624 N/m

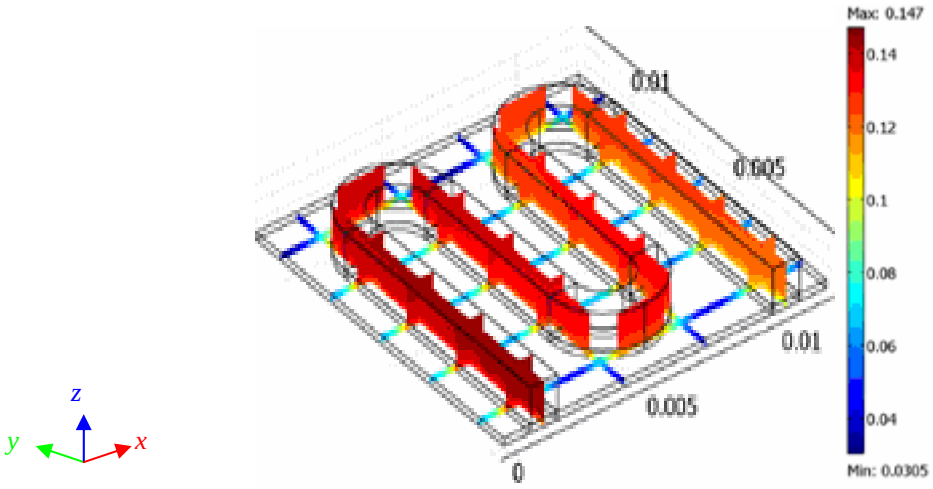

Figure 22: Mass fraction of oxygen in the channel and porous cathode.

Figure 23 displays a top view of current-density distribution throughout the entire active layer. The current density is significantly higher below the gas channels. A maximum current density of 2400 kA/m^2 is reached under the center of the channel in the inlet region. The lowest current density is only 420 kA/m^2. This huge difference in current density is might be due to the uneven utilization of the active layer [3]. It indicates that the thickness of the diffusion layer might need to be increased to optimize the electrode's performance. We studied the water management by plotting the water fraction in the gas channel as shown in Figure 24. We can see clearly from Figure 24 that the water fraction increases significantly in the electrode. It reaches a maximum value of 0.74 in the corner at the top of the Figure 24. It is probably the fact that water droplets would start forming in this region. To avoid this problem, in the design we should decrease the inlet water fraction and increase the thickness of the diffusion layer.

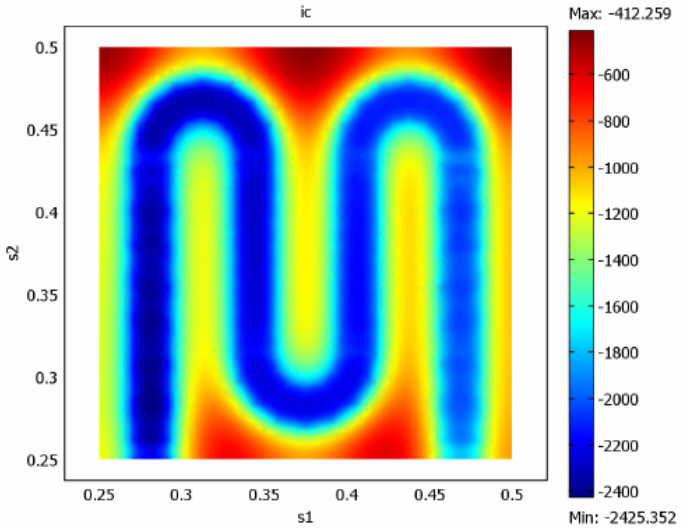

Figure 23: Top view of the current-density distribution on the surface of the catalytic active layer.

Figure 25 represents the resulting gas-velocity (gas phase) distribution in the gas channel. The applied pressure difference of 25 Pa resulted in a maximum gas velocity of

approximately 2 m/s. A typical laminar flow profile is present in the straight sections. In the curved sections, on the other hand, the gas velocity distribution is asymmetric, resulting in an asymmetric concentration of gas distribution there.

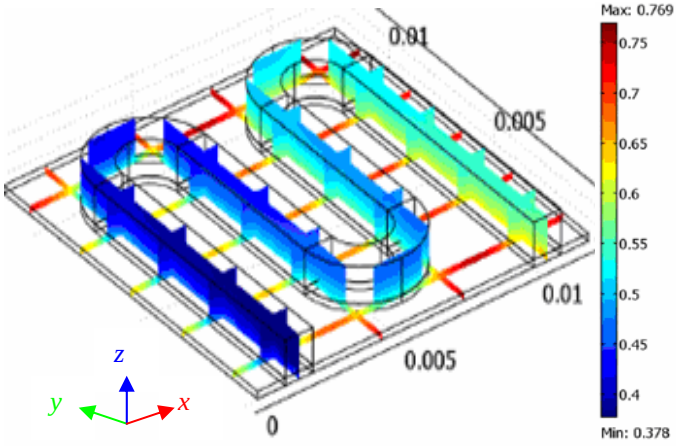

Figure 24: Weight fraction of liquid phase (water) in the cathode gas.

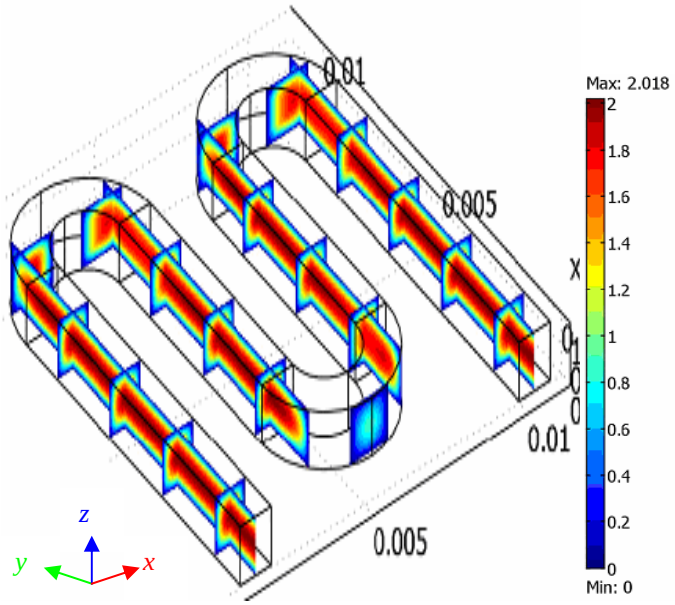

Figure 25: Gas-velocity (gas phase) distribution in the gas channel for a 25 Pa pressure drop between the inlet and outlet.

2.10: Multiphase CFD flow model validation

The water and thermal management issues of an operational PEM fuel cell are critical to enhancing cell performance because electrode flooding and membrane dehydration results in degradation of cell performance. For better understanding, we compare results of our multiphase porous flow model with the results available in the literature. Figure 26 presents the comparison of distribution of O_2 concentration in the cathode channel obtained using our multiphase porous flow

model simulation (Fig 26a) with those obtained (Fig 26b) by Wang and Wang [17]. The color bar represents the concentration from highest (red) to lowest (blue) and the black arrow denotes cathode gas velocity.

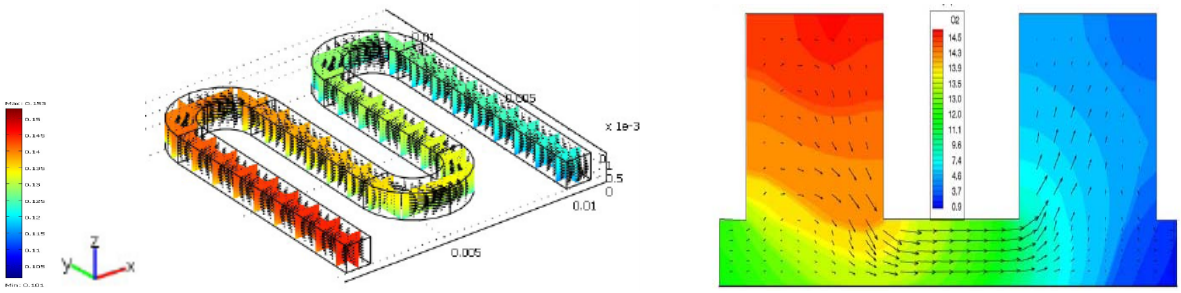

(a) **(b)**

Figure 26: Concentration distribution of gas phase (O_2) in the cathode channel. (a) 3D simulation of cathode with present multiphase model, (b) 2D model simulation of Wang and Wang [17]. Black arrow indicates cathode gas velocity inside the channel.

As seen from Figure 26, the O_2 concentration at the cathode inlet is the highest since fresh humidified air is supplied at the cathode. From Figure 26, we see that a substantial amount of oxygen depletion in the regions far away from the inlet gas channel which resulted the high current density. Comparing Figures 26a and 26b we see that the O_2 depletion trend along the gas channel are qualitatively similar or comparable in terms of distribution along the channel as shown in colors. Thus we obtained a qualitative agreement between our multiphase flow model and that of the results reported by Wang and Wang [17]. In Figure 26b, we see a higher amount of O_2 concentration (see the values at the color bar (Fig 26b)) at the inlet. In our simulation, we only simulated PEM fuel cell cathode. Addition of anode portion into our simulation will be considered in the next step.

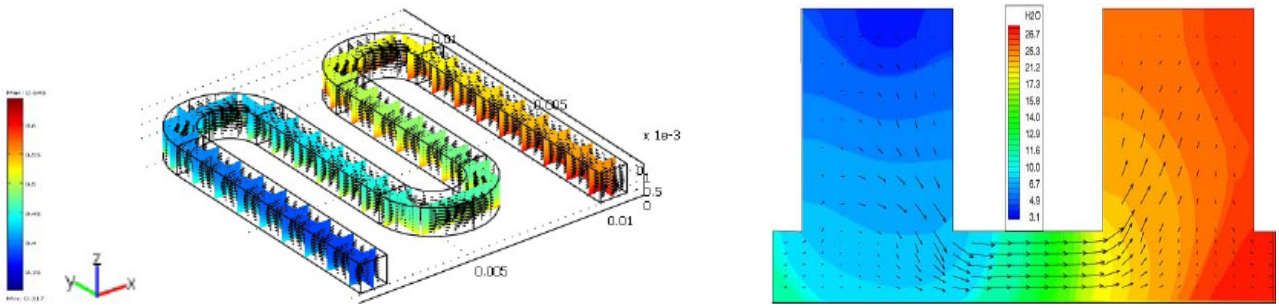

(a) **(b)**

Figure 27. Concentration distribution of liquid phase (water - H_2O) in the cathode channel. (a) 3D simulation of cathode with present multiphase model, (b) 2D model simulation of Wang and Wang [17]. Black arrow indicates cathode gas velocity inside the channel.

Figure 27 presents the concentration distribution of liquid phase (H_2O) in the cathode channel obtained using our multiphase porous flow model simulation (Fig 27a) with those obtained (Fig 27b) by Wang and Wang [17]. The color bar represents the concentration from highest (red) to lowest (blue) and the black arrow denotes cathode gas velocity. From Figure 27, we see that the concentration of liquid phase (water) at the cathode inlet is the lowest since humidified air which has small water vapor content only (no liquid water) is supplied at the cathode. The liquid phase

concentration is increasing along the gas channel from the inlet to the outlet due to oxygen reduction reaction (ORR) over the cathode electrode to produce liquid phase (water). The depletion of O_2 along the cathode electrode produced liquid water through the electrochemical reaction at the cathode. Hence the liquid phase concentration increased along the gas channel. From Figure 27, we see that the liquid phase concentration increases substantially in larger amount in the regions far away from the inlet gas channel. Comparing Figures 27a and 27b, we see that the trend of increasing liquid phase concentration along the gas channel is similar. This indicates a qualitative agreement between our multiphase flow model and that of the results reported by Wang and Wang [17], although in Figure 27b we see a higher concentration of liquid phase (see the values at the color bar (Fig27b)) at the outlet because of the requirements of maintaining the balance of the anode/cathode gas ratio. A higher supply of reactant gases which increases the reaction rate results in higher liquid phase concentration. Liquid phase concentration increases along the far end of the channel is due to the production of liquid water through electro-chemical reaction. In our simulation, we only simulated PEM fuel cell cathode. Addition of anode portion into our simulation will be considered in the next step. The parametric values used in the simulation for the results presented in Figures 26 and 27 are listed in the Table 3 below [17]. The predictions obtained from the two-phase flow model (Fig. 26a and 27a) will be beneficial to improve PEM fuel cell designs.

Table 3: Geometrical and Physical parameters used in the simulation for Figures 26 and 27.

Quantity/Parameter	Value
Gas channel depth	1 mm
Gas channel height	1 mm
Gas channel width	1 mm
Diffusion layer thickness	0.3 mm
Catalyst layer thickness	0.01 mm
Pressure difference between cathode inlet and outlet	0.2 atm
Reference current density	1.0 amp/cm^2
RH (Relative Humidity) of cathode inlet	90%
Temperature of fuel cell cathode	80^oC
Porosity of the cathode GDL [17]	0.6
Porosity of catalyst layer [17]	0.4
Permeability of the GDL, K (m^2) [17]	10^{-12}
O_2 diffusivity in cathode gas at standard condition [18]	$3.2348x10^{-5}$
H_2O diffusivity in cathode gas at standard condition [18]	$7.35x10^{-5}$

Figure 28 represents the gas phase velocity along the cathode channel. Red arrow indicates velocity vector. Figure 28a represents the simulation results of gas phase velocity using our developed multiphase porous flow model and Figure 28b represents those of Hwang [18]. The

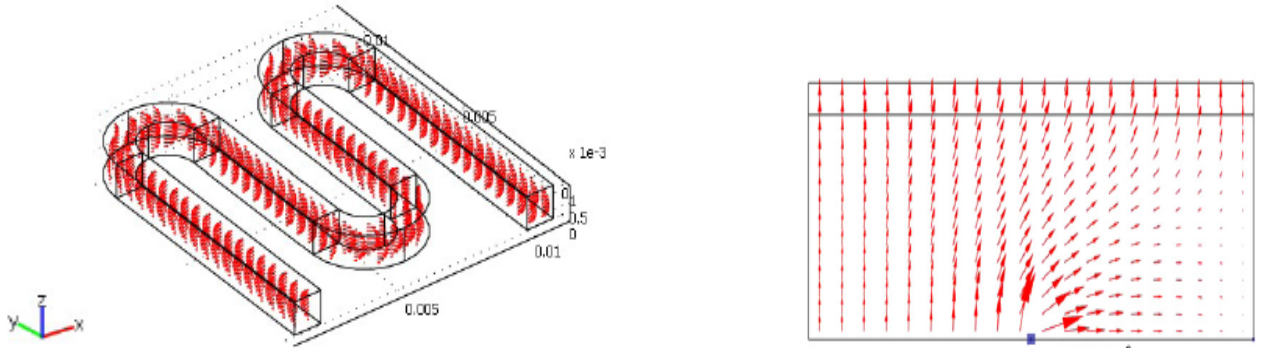

Figure 28. Distribution of gas-phase velocity in the cathode gas mixture. (a) 3D multiphase model present and (b) 2D two-phase model [18]. The red arrow indicates gas-phase velocity.

gas-phase velocity vectors shown in Figure 28 induce the gaseous mixture from the flow channel into the porous cathode. This is in contrast with the results obtained by the single-phase model [17] in which the gaseous-mixture velocity is directed from the porous cathode to the flow channel. Comparing Figures 28a and 28b we see that the trend of gas phase velocity in the cathode channel is similar or comparable. This concludes a qualitative agreement between our multiphase flow model and that of the results reported by Hwang [18]. The parametric values used in the simulation for the results presented in Figure 28 are listed in the Table 4 below.

Table 4: Parametric values used for porous-electrochemical variables in the model simulation.

Parameter	Value
Gas channel depth	1 mm
Gas channel height	1 mm
Gas channel width	1 mm
Diffusion layer thickness	0.3 mm
Catalyst layer thickness	0.01 mm
Pressure difference between cathode inlet and outlet	0.2 atm
Reference current density	0.5amp/cm^2
RH (Relative Humidity) of cathode inlet	90%
Temperature of Fuel cell cathode	80^oC
Porosity of the cathode GDL [18]	0.48
Porosity of catalyst layer [18]	0.42
Permeability of the GDL, K (m^2) [18]	$2.55x10^{-13}$
Reference mole fraction of O_2 [18]	3.6641 $molm^{-3}$
Reference mole fraction of H_2O [18]	0.0703 $molm^{-3}$
Inlet water-vapor mass fraction	0.0198
Inlet O_2 mass fraction	0.2284
Inlet N_2 mass fraction	0.7518

For improving CFD model predictions especially for an operational PEM fuel cell environment, we simulated both a single-phase CFD model [14] and our two-phase CFD model using finite element analysis tools.

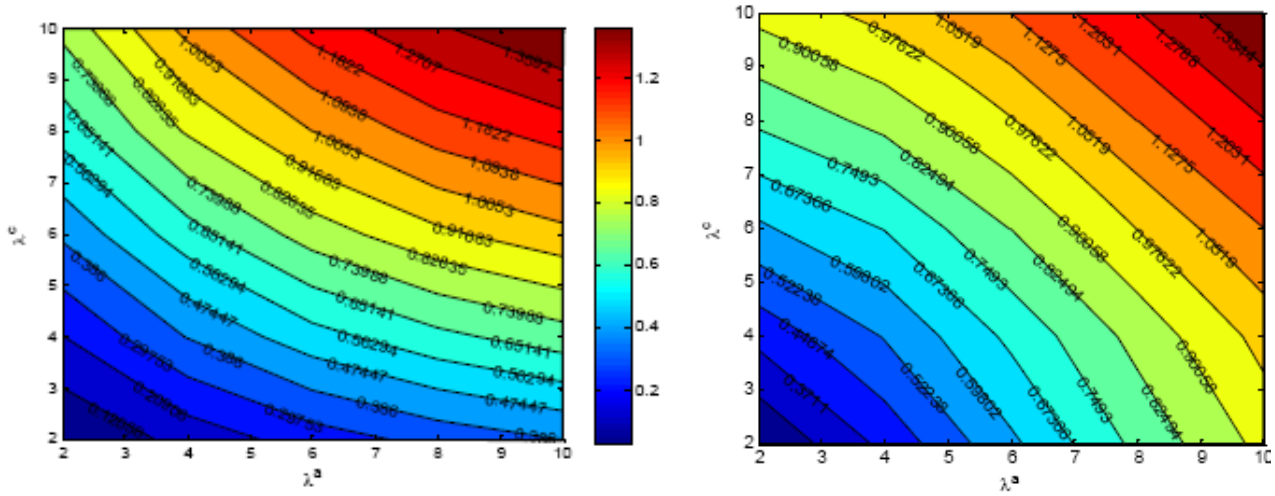

Figure 29. Current density distribution across the membrane at 80°C. λ^a and λ^c denotes the membrane water content at the anode and cathode side of the membrane respectively. (a) single phase model [14] and (b) two-phase CFD model.

Figure 29 represents the current density distribution across the membrane at 80°C for different anode and cathode side membrane humidification. Both single phase (Fig 29A) and two-phase model (Fig 29B) simulations are presented in Figure 29. We can see significant improvement in current density predictions in two-phase model (Fig 29B) compared to single phase model (Fig 29A), especially at low membrane water content. The predictions obtained from two-phase flow model (Fig 29B) will be beneficial to improve air-breathing fuel cell designs.

2.11: Conclusions (multiphase CFD flow model simulation)

In this study, we performed computer simulation of a two-phase flow model and analyzed the results mostly related to the PEM fuel cell cathode to improve understanding regarding water management phenomena within an operational PEMFC's conditions. Both liquid and gas phases are considered in the model. The model is solved numerically under different parametric conditions in terms of water management issues in order to improve cell performance. The results obtained from two-phase flow model simulations show improvement in cell performance compared to the results of a single phase flow model available in the literature. The quantitative information obtained from the two-phase model simulation results is helpful in designing improvement of PEMFC for improved operational efficiency and performance. We gained insight into the water and thermal management issues in an operating PEM fuel cell by analyzing the results obtained through multiphase CFD flow model analysis. This information is critical to understand the fundamental physics of water and thermal management phenomena in a single PEM fuel cell as well as fuel cell stacks. Although the DOE deliverables of our project up-to-date have been achieved, additional attributes are required for the implementation of CFD two-phase porous flow model in a complete single fuel cell as well as fuel cell stacks for improvement of water and thermal management design strategies and it would be done in a future study subject to the availability of external research funds.

3.: Development of a control strategy for real time optimization of low temperature PEM fuel cell stack

3.1: Abstract

A robust control strategy which ensures optimum performance is crucial to proton exchange membrane (PEM) fuel cell development. In a PEM fuel cell stack, the primary control variables are the reactant's stochiometric ratio, membrane's relative humidity and operating pressure of the anode and cathode. In this study, a 5 kW (25-cell) PEM fuel cell stack is experimentally evaluated under various operating conditions. Using the extensive experimental data of voltage-current characteristics, a feed forward control strategy based on a 3D surface map of cathode pressure, current density and membrane humidity at different operating voltages is developed. The effectiveness of the feed forward control strategy is tested on the Green-light testing facility. To reduce the dependence on predetermined system parameters, real-time optimization based on extremum seeking algorithm is proposed to control the air flow rate into the cathode of the PEM fuel cell stack. The quantitative results obtained from the experiments show good potential towards achieving effective control of PEM fuel cell stack.

3.2: Experimental testing of control algorithm

The Green-light test stand, in the center for fuel cell systems and powertrain integrations at Kettering University, developed by Hydrogenics shown in Figure 30 was used for testing a 5kW low temperature PEM fuel cell stack (Ballard Mark9 SSL stack). The developed control strategy was validated experimentally by using Green-light test stand and Ballard Mark9 SSL 5kW stack.

Figure 30: Green-light test stand with Ballard Mark9 5kW (stack not shown due to proprietary issue) low temperature PEM fuel cell stack.

3.3: Effect of Pressure

The performance of the fuel cell for an anode stoich of 1.2 and cathode stoich of 2.0 are shown in Figure 31. There is a minimum stack flow requirement that has to be maintained and if the stoichiometric requirement is below the minimum flow rate the minimum flow rate overrides the stoichiometric requirement. Hence at current densities lower than 200mA/cm^2, the stoichiometry is always higher than 1.2 at anode and 2.0 at cathode. According to the operating conditions of Ballard 5kW stack, there is a minimum pressure drop requirement from the stack inlet to the outlet to meet the fuel supply requirements. At higher current densities, i.e. at higher fuel flow rate, the pressure drop is larger than 0.6 bar; hence the lowest pressure to operate the fuel cell at higher current densities was chosen to be 1.72 bar. The stack is rated for a maximum pressure of 2.5 bar, so the maximum operating pressure was chosen to be 2.42 bar. There is also a 0.07 bar

pressure differential between the anode and cathode pressures. The pressure stated in this report refers to the anode pressure and the cathode pressure can be obtained by subtracting 0.07 bar from the anode pressure. Voltages plotted are the mean cell voltages of the 25 cell stack unless stated otherwise.

As seen from Figure 31, the fuel cell performs better at higher pressure. The operating pressure influences the performance of the fuel cell. Higher pressures ensure higher partial pressure of the fuel and oxidant which improves the performance of the fuel cell. Figure 31a shows the effect of pressure variations on the polarization curve while the stack is operated at 100% relative humidity. Figure 31b represents the effect of pressure variations on the polarization curve while the stack is operated at 70% relative humidity. Comparing Figure 31a and 31b, it can be found that the variation in cell performance is more pronounced at lower humidity compared to at higher humidity.

3.4: Effect of relative humidity

To study the effect of relative humidity (RH), the fuel cell stack performance was tested at four different humidity conditions - 70%, 80%, 90% and 100% respectively. The variation in cell performance at four different RH is shown in Figure 32. Because of the humidification system setup on the green-light test stand, there is a temperature fluctuations between 1~2^{o}C on the anode and cathode dew point sensors. Hence variation in humidity was maintained at 10%.

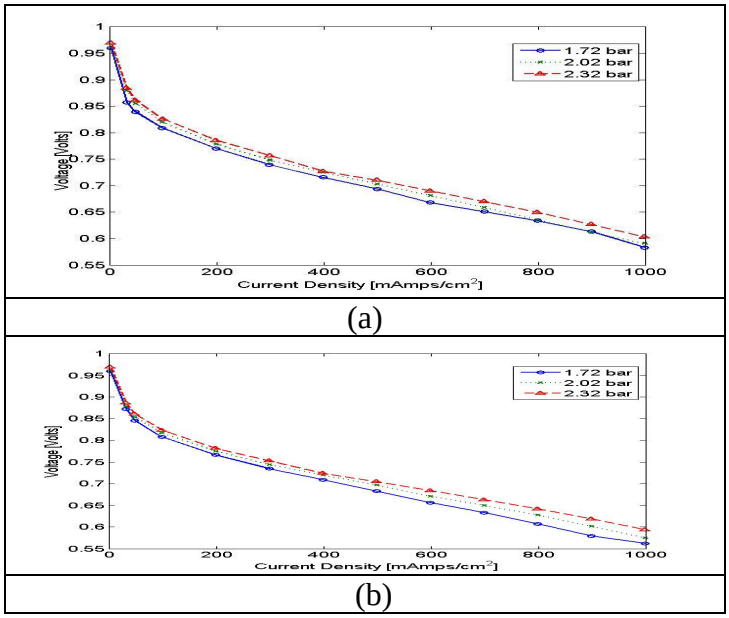

Figure 31: Effect of pressure on the polarization curve, for three different pressures - 1.72, 2.02 and 2.32 bar: (a) At higher relative humidity=100%, (b) At lower relative humidity =70%.

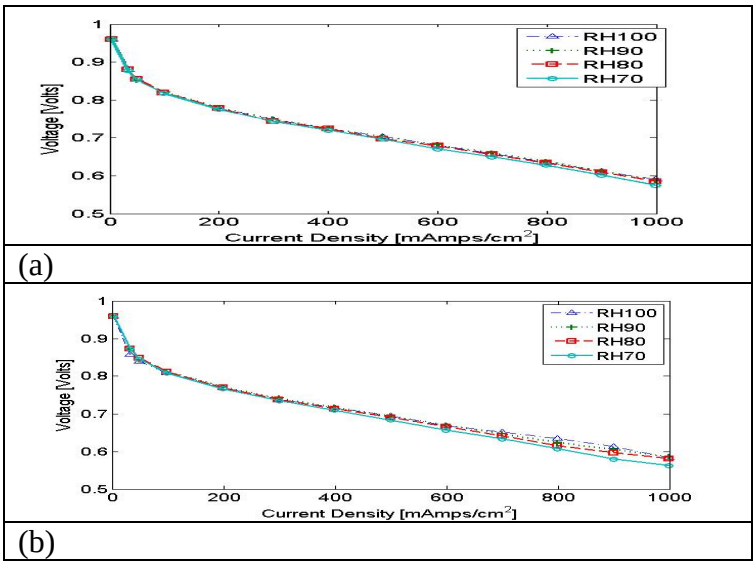

Figure 32: Effect of Relative Humidity on the polarization curve, for four different humidities 70%, 80%, 90% and 100%: (a) At higher pressure =2.32 bar, (b) At lower pressure=1.72 bar.

To maintain stack health (i.e. MEA well-hydrated) prolonged operation below 70% RH was avoided. From Figure 32, we can see that the variations in I-V curves is more pronounced at lower RH compared to higher RH at high current densities. It implies that accurate control of relative humidity is essential in the PEM fuel cell operation. If the relative humidity is too high, there is a risk of condensation and stack flooding. At lower humidity the membrane is not properly humidified and its conductivity goes down. As a consequence the cell performance decreased.

3.5: Implementation of control algorithm using CFD model

Using the multi-phase CFD model results given in Figures 21~29, a 3D surface map of relative humidity, pressure at the cathode and current density at different voltages of the PEM fuel cell stack was developed and tested for a 5kW stack.

As seen from Figures 31 and 32, there is a considerable effect in PEM fuel cell stack's performance with both humidity and pressure variations. The polarization data for different pressures and relative humidities obtained experimentally, as shown in Figures 31 and 32, were used as a base case to evaluate the control algorithm for PEM fuel cell stack. An operating current density range of 200 -700mA/cm^2 was chosen to implement the control strategy. At current densities lower than 200mA/cm^2 the stoichiometry was to be greater than 1.6 on the anode and 2 on the cathode side to maintain the minimum flow rate required as per Ballard's specification. To avoid prolonged operation at higher current densities an upper limit of 700mA/cm^2 was chosen. However, the control strategy can be extended and implemented at higher current densities too. From these polarization data a 3D surface maps of relative humidity, pressure and current density at different voltages were obtained.

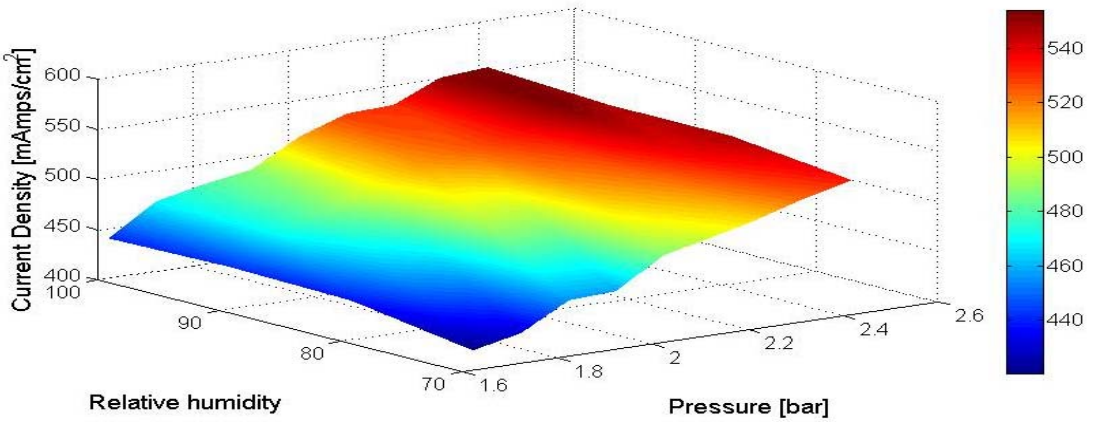

Figure 33: Surface map of the variation of current density with pressure and relative humidity at a constant voltage of 0.7V.

Figure 33 shows the surface map for a voltage of 0.7V. At this voltage, the current density varies from 440-550 mA/cm^2. Using the Current density, we can calculate the power from the following equation as:

$$P_{stack} = I_{stack} * n * V_{op} * A \quad (61)$$

where n =number of cells in the stack and A=cross sectional area of the fuel cell. This gives us the range of power at which we can operate the fuel cell stack at this voltage. For different voltages, we can calculate the power and we can obtain a lookup table for the power demand with operating voltage. On the green-light test stand, the fuel and oxidant gases were supplied at a higher pressure. But in reality, the gases have to be compressed in a compressor before they are fed to the fuel cell stack. The energy needed for compression has to be supplied by the fuel cell itself. To obtain the power demand for the compressor CHEMCAD simulation software was used to calculate the power based on the anode and cathode flow rates and compression ratios. By subtracting the compressor power from the fuel cell stack power we can obtain the net power that can be provided by the fuel cell stack. Figure 34 shows both the stack power and net power for a cell voltage of 0.7V. Based on the net power, we can develop a lookup table between the operating voltage and power demand. This lookup table is shown in Table 5.

Table 5: Lookup Table for net power and operating voltage.

Minimum power	Maximum Power	Operating Voltage
1200	1500	.76
1500	1800	.74
1800	2100	.72
2100	2300	.70
2300	2500	.68

So, for a particular power demand we can calculate the optimum operating pressure and humidity. The feed forward control strategies developed here calculates this optimum operating

point and send it as an input to the fuel cell stack. The steps followed to obtain the optimum operating points are:

(1) Determine the power demand
(2) Calculate the appropriate operating voltage (V_{op}) based on the range of power demand from the lookup table
(3) From the surface map for net power at the selected voltage, calculate the minimum pressure Pr_{op} and Relative humidity RH_{op} at which you can get the required power demand.
(4) From the surface map we can calculate the corresponding P_{stack} for the selected operating pressure and relative humidity (Pr_{op}, RH_{op}).
(5) Calculate I_{stack} from P_{stack} using equation (61) and send I_{stack}, Pr_{op}, RH_{op} as input to the system.

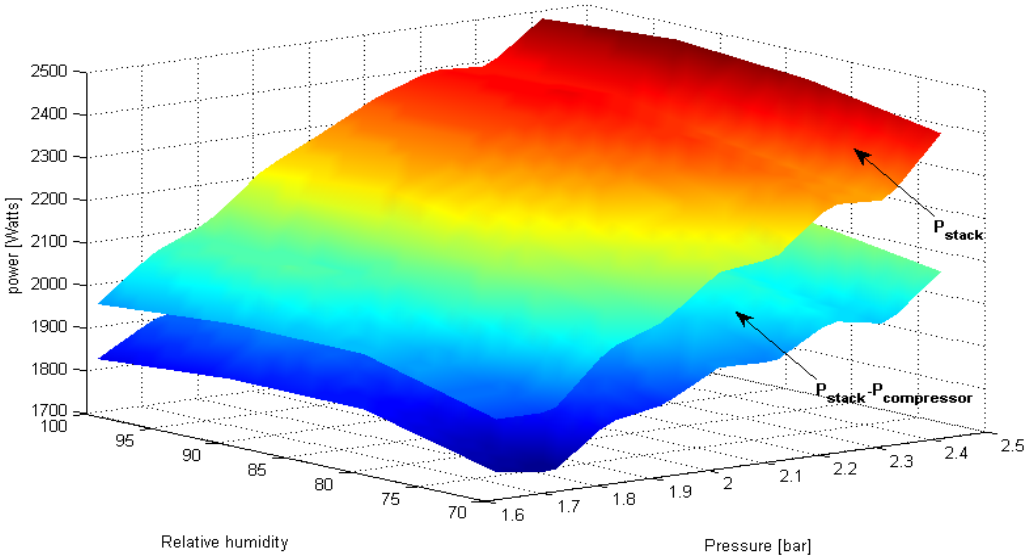

Figure 34: Surface map of stack power and the net power that can be provided by the stack at a voltage of 0.7V.

The present humidification system on the green-light test stand has a large time constant. Hence it is not possible to change the relative humidity dynamically, so the stack was operated at a constant RH. The control algorithm was modified to search along a particular RH. Figure 35 shows the control algorithm implemented for a RH of 90%. The control algorithm was implemented for a step input in power from 1300 to 2500 watts. The net power and the corresponding stack power are shown in Figure 6 where the change in pressure, voltage and current density are also shown.

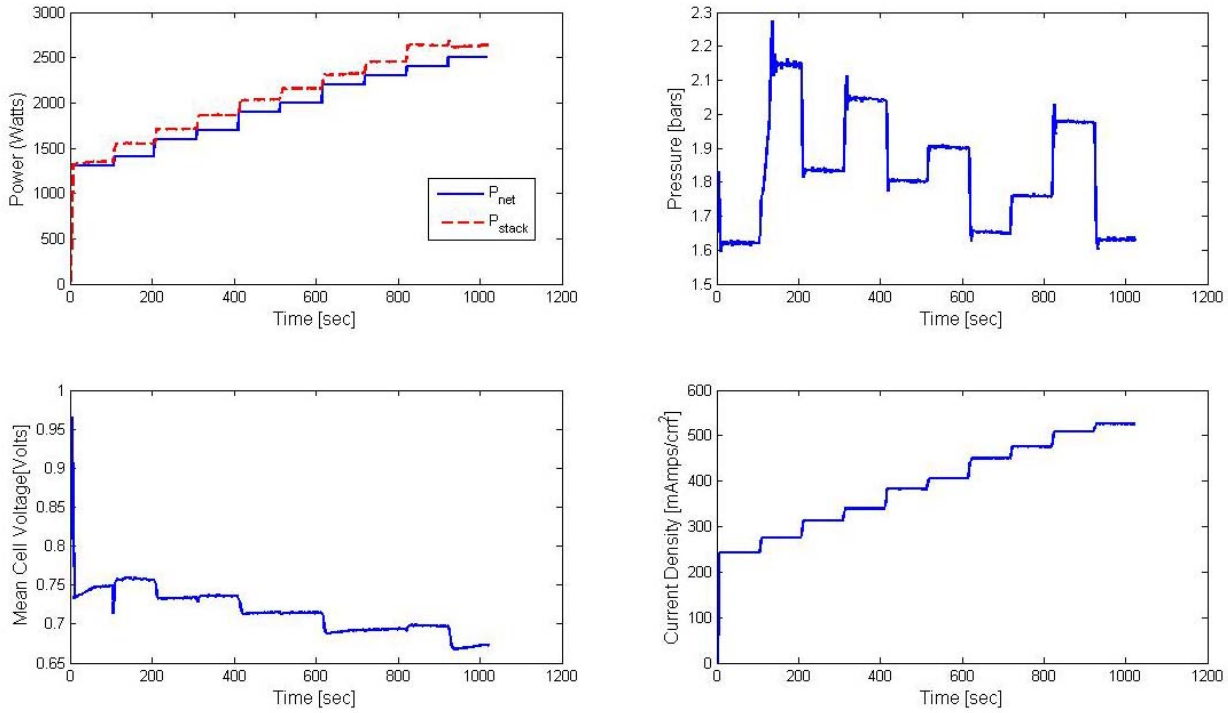

Figure 35: Controller performance for a step-up power demand varying between 1.3 to 2.5 kW.

For a gas of known or desired humidity, we can calculate the pressure to operate the fuel cell stack from the 3D surface map of current density, humidity, and pressure. Then the pressure can be used in a feed forward control algorithm to meet the power requirement. As such, we can operate the fuel cell stack with a humidity driven power management strategy. For a gas of known humidity, for example 90%, the control algorithm can be modified to search along a particular RH.

3.6: Conclusions (CFD control algorithm development)

A 5kW PEMFC stack was evaluated at different operating pressures and relative humidity. 3D surface maps at different voltages were developed with relative humidity, cathode pressure and current density. A control strategy based on the surface maps was evaluated experimentally and was shown to provide meaningful practical results. A real-time optimization method is being developed, which does not require extensive testing or knowledge of system parameters.

4. References

[1] Nafion®, E.I. DuPont de Nemours and Company, U.S.A. (2004).

[2] H. L.Yeager, A. Steck,, Cation and Water diffusion in Nafion ion exchange membranes influence of polymer structure, J. Electrochem. Soc. 128(9), 1880-1884 (1981).

[3] Larminie J. and Dicks A., *Fuel cell systems explained*, John Willey & Sons, New York (2000).

[4] Beholz, L. G., "Process for Producing Painted Polymeric Articles," *US Patent No.* 6,100,343 (2000).

[5] Beholz, L. G., "Apparatus for Treating Polymeric Material to Improve Surface Adhesion," US Patent No. 7,022,291 (2006).

[6] Susanta K. Das and K. Joel Berry, "Two-cell theory to measure membrane resistance based on proton flow: Theory development and experimental validation," *Journal of Power Sources*, 173, 909 (2007).

[7] J. S. Wainright, M. H. Litt, R. F. Savinell, In *Handbook of Fuel Cells*, Vielstichm W, Lamm A, Gasteiger HA (Eds.), John Wiley & Sons Ltd, New York, 3, 436 (2003).

[8] R. J. Gillespie, E. A. Robinson, In Nonaqueous Solvent Systems, T. C. Waddington (Ed.) Academic Press New York, 117-210 (1965).

[9] Abriola L. M. and Pinder G. F., "A multiphase approach to the modeling to porous media contamination by organic compounds 1. Equation development," *Water Resour. Res*., 21, 11-18 (1985).

[10] Wang C. Y. and Cheng P., "A multiphase mixture model for multiphase, multi-component transport in capillary porous media – I: model development," *Int. J. Heat Mass Transfer*, 39, 3607-3618 (1996).

[11] Bird R. B., Stewart W. E. and Lightfoot E. N., "Transport Phenomena," Second ed., *John Wiley and sons Inc.*, New York (2002).

[12] Vafai K. and Tien C. L., "Boundary and inertia effects on flow and heat transfer in porous media," *Int. J. Heat Mass Transfer*, 24, 195-203 (1981).

[13] Wang C. Y. and Gu W. B., "Micro-macroscopic coupled modeling of batteries and fuel cells – I. Model development," *J. Electrochem. Soc.*, 145(10)**,** 3407-3417 (1998).

[14] Springer, T.E., Zawodzinski, T. A. and Gottesfeld S., "Polymer electrolyte fuel cell model," *J. Electrochem. Soc.*, 138, 2334 (1991).

[15] Leverett M. C., "Capillary behaviour in porous solids," *Trans. AIME*, 142, 152-169 (1941).

[16] Natarajan D. and Nguyen T. V., "A two-dimensional, Two-phase, multicomponent, transient model for the cathode of a proton exchange membrane fuel cell using conventional gas distributors," *J. Electrochem. Soc.*, 148, A1324-A1335 (2001).

[17] Wang, Y. and Wang C. Y., *J. Power Sources*, 147, 148-161 (2005).

[18] Hwang, J. J., Chao, C. H., Ho, W. Y., Chang, C. L., Wang, D. Y., *J. Power Sources*, 157, 85 (2006).

[19] Pukrushpan, J. T., Stefanopoulou, A. G., Peng, H., "*Control of Natural Gas Catalytic Partial Oxidation for Hydrogen Generation in Fuel Cell Applications*," Proceedings of the American Control Conference, Denver, CO (2003).

[20] Panini Kolavennu, Susanta K. Das and K. Joel Berry, "Control Oriented Model with Improved Membrane Hydration of PEM Fuel Cell Stacks" Proceedings of the Second European Fuel Cell Technology and Applications Conference Rome, Italy (2007).

[21] Feroldi, D., Serra, M., and Riera, J., "Performance improvement of a PEMFC system controlling the cathode outlet air flow, " *Journal of Power Sources*, 169, (2007).

[22] Judith O'Rourke, Murat Arcak, Manikandan Ramani "Real time optimization of net power in a fuel cell system," *Journal of power sources*, 187 (2009).

5. Product development under the award and technology transfer activities

Publications

Peer reviewed journal publications

1. Susanta K. Das, K. J. Berry, J. Hedrick, Ali R. Zand, and L. Beholz, "Synthesis and Performance Validation of a Polymer Mesh Supported Proton Exchange Membrane for Fuel Cell Applications," *Journal of Membrane Sciences*, 2009 (submitted – under review).

2. Susanta K. Das, Panini Kolavennu, J. Hedrick, Beholz, L., Ali R. Zand and K. J. Berry, "Synthesis and Characterization of a Composite Membrane for Polymer Electrolyte Fuel Cell," *Journal of Fuel Cell Science and Technology*, vol. 6, p. 011021-1~011021-6 (2009).

3. Susanta K. Das, and K. J. Berry, "Two-cell theory to measure resistance of proton exchange membrane based on proton flow: Theory development and experimental validation," *Journal of Power Sources*, Vol. 173, p. 909-916 (2007).

Peer reviewed Conference publications

1. Panini Kolavennu, Susanta K. Das, and K. J. Berry, "Experimental Evaluation of a control strategy for real time optimization of low temperature PEM fuel cell stack," *Proc. ASME International Mechanical Engineering Congress and Exposition* held on November 13-19, Lake Buena Vista, Florida, USA, Paper No. 12031, Section: Emerging Technologies (in Structural and Materials Aspects of Alternative Energy Systems), p. 1-4 (2009).

2. Susanta K. Das and K. J. Berry, "CFD Analysis of a Two-Phase Flow Model for a Low Temperature Proton Exchange Membrane Fuel Cell," *Proc. ASME 6th International Fuel Cell Science, Engineering & Technology Conference* held on June 16-18, Denver, Colorado, USA, Paper No. 65212, Section: Cell, Stack and System Modeling, p. 1-10 (2008).

3. Susanta K. Das and K. Joel Berry, "Proper Flow Channel Design for Uniform Distribution of Gas in PEM Fuel Cell Stacks," *Proc. The Second European International Fuel Cell Technology and Applications Conference* held on December 11-14, Rome, Italy, p. 197-198 (2007).

4. Panini Kolavennu, Susanta K. Das and K. Joel Berry, "Control Oriented Model with Improved Membrane Hydration of PEM Fuel Cell Stacks," *Proc. The Second European International Fuel Cell Technology and Applications Conference* held on December 11-14, Rome, Italy, p. 199-200 (2007).

5. Etim U.Ubong and Susanta K. Das, "Validating Theoretical Models in Two PEM Fuel Cells Categories," *Proc. The Second European International Fuel Cell Technology and Applications Conference*, held on December 11-14, Rome, Italy, p. 193-194 (2007).

6. Susanta K. Das, Beholz, L., Hendrick, J., Ali R. Zand and K. Joel Berry, "Advanced Proton Exchange Membrane for Fuel Cell Applications," *Proc. Fuel Cell Seminar*, held on October 15-19, San Antonio, Texas (2007).

7. Susanta K. Das, Panini Kolavennu, J. Hedrick, K. J. Berry and Etim U. Ubong, "Improved Performance of Proton Exchange Membrane Materials for Fuel Cell Applications," *Proc. 5th ASME International Fuel Cell Conference*, held on June 18-20, New York (2007).

8. Etim U. Ubong and Susanta K. Das, "3D Modeling with COMSOL Multiphysics and Experimental Validation of PEMFC with Two Membranes," *Proc. Fuel Cell Seminar*, held on October 15-19, San Antonio, Texas (2007).